



# A Physically Integrated GNN Surrogate for Microbially-Mediated Kinetic Reactive Transport: PHYGNET

Jinbo Wang<sup>1,2</sup>, Kunfeng Zhang<sup>3</sup>, Walter Illman<sup>4</sup>, Shuai Chen<sup>1,2</sup>, Mingzhu Liu<sup>1,2</sup>

<sup>1</sup> School of Water Resources and Environment, China University of Geosciences (Beijing), Beijing 100083, China.

5 <sup>2</sup> Key Laboratory of Groundwater Conservation of Ministry of Water Resources, China University of Geosciences (Beijing), Beijing 100083, China.

<sup>3</sup> CNPC Research Institute of Safety & Environment Technology, Beijing, 102206, China.

<sup>4</sup> Department of Earth & Environmental Sciences, University of Waterloo, Waterloo, ON, N2L 3G1, Canada.

*Correspondence to:* Mingzhu Liu (liumz@cugb.edu.cn).

10 **Abstract.** Reactive transport modelling (RTM) is essential for subsurface environmental management but is fundamentally constrained by traditional geochemical solvers. These solvers incur prohibitive computational costs and frequently suffer from numerical instabilities such as convergence failures, particularly in microbially-mediated kinetic reaction systems. While machine learning surrogates offer acceleration, they often lack physical consistency when dealing with stiff biogeochemical dynamics. Here we propose PHYGNET (Physically GNN Network), which maps microbial reaction networks into a directed  
15 graph by representing species and reactions as nodes and edges. It embeds Monod-type kinetics within a physics layer to enforce mass conservation and thermodynamic hierarchies, and incorporates a residual corrector for refinement. By successfully coupling with COMSOL, PHYGNET demonstrates the capability to execute full reactive transport simulations. Benchmark tests reveal that, in contrast to the severe super-linear time penalties faced by traditional solvers at engineering scales, PHYGNET maintains stable sub-linear scaling via tensor parallelism. At a scale of  $10^5$  grid nodes, PHYGNET achieved  
20 an acceleration (up to 3524-fold) without numerical crashes. Furthermore, its escalating speedup ratio establishes a “small-sample training, ultra-large-scale inference” paradigm that effectively offsets initial data generation costs. Overall, PHYGNET provides an efficient and physically consistent framework for accelerating Monod-type microbial reactive transport simulations, offering a practical pathway for large-scale environmental applications.

## 1 Introduction

25 Reactive transport modelling (RTM) provides a process-based framework to quantitatively describe and predict the distribution of chemicals across spatial and temporal scales, while offering a rigorous means to test our understanding of the underlying processes and controlling factors (Meile and Scheibe, 2019; Steefel et al., 2015). Among these processes, microbially mediated reactions constitute a central driver of biogeochemical cycling, governing the transformation and redistribution of key elements under thermodynamically constrained conditions (Falkowski et al., 2008; Meile and Scheibe, 2019). To quantitatively resolve  
30 these dynamics, Monod-type kinetics, often implemented via Michaelis-Menten formulations, represent a widely adopted and



foundational approach within the RTM framework (Johnson and Goody, 2011). These formulations explicitly capture substrate limitation, electron acceptor competition, and nonlinear transitions between metabolic regimes, enabling RTMs to reproduce complex redox zonation and pathway switching. Consequently, RTMs equipped with these biogeochemical modules have become indispensable not only for predictive applications, such as groundwater remediation (Brookfield et al., 2023; Prommer and Stuyfzand, 2005), but also for advancing mechanistic understanding of thermo-hydro-mechanical-chemical-biological (THMCB) coupling in geological systems (Mayer et al., 2002).

However, this mechanistic fidelity comes at a significant computational cost, as Monod-type formulations introduce strong nonlinearity and tight coupling among species. By expressing reaction rates as nonlinear functions of multiple substrates, electron acceptors, and environmental variables, these models generate highly coupled and stiff systems of ordinary differential equations. As a consequence, the geochemical reaction module becomes the primary computational bottleneck in RTMs (Laloy and Jacques, 2022; Silva et al., 2025), often requiring orders of magnitude more computational effort than transport calculations due to repeated nonlinear iterations and convergence control (De Lucia and Kühn, 2021; He et al., 2015). In large-scale or highly resolved simulations, these costs escalate dramatically and are frequently accompanied by numerical instabilities, including convergence failures under extreme chemical gradients (Deng et al., 2025). Such limitations severely restrict the feasibility of critical analyses (such as uncertainty quantification, parameter estimation, and inverse modelling), thereby hindering the broader application of RTMs in both scientific investigation and real-world decision-making (Fotherby et al., 2023; Shi et al., 2014). This fundamental trade-off between mechanistic fidelity and computational tractability remains a central challenge in modern reactive transport modelling.

By expressing reaction rates as functions of multiple substrates and environmental factors, these models generate highly coupled and stiff systems of ordinary differential equations, making the geochemical reaction module the primary computational bottleneck in RTMs (Laloy and Jacques, 2022; Silva et al., 2025), where nonlinear resolutions can require orders of magnitude more effort than transport calculations (De Lucia and Kühn, 2021; He et al., 2015). This cost escalates further when reaction networks include sequential electron-acceptor pathways, such as aerobic respiration, denitrification, sulfate reduction, and methanogenesis, which introduce strong thermodynamic ordering, tight species coupling, and near-discontinuous redox transitions. Moreover, complex biogeochemical reaction networks can introduce numerical stiffness and convergence difficulties (Deng et al., 2025). These prohibitive computational expenses severely limit the feasibility of essential analyses, such as uncertainty quantification, parameter optimization, and inverse modelling, creating a significant barrier to their widespread use in decision-making and comprehensive system analysis (Fotherby et al., 2023; Shi et al., 2014).

In response to these challenges, researchers have increasingly turned to artificial intelligence (AI) surrogates to accelerate RTMs (De Lucia and Kühn, 2021; Demiret et al., 2023; Jatnieks et al., 2016; Sprocati and Rolle, 2021). Parallel developments in groundwater science demonstrate the maturity of machine learning (ML) for subsurface prediction and inference, spanning groundwater-level forecasting (Kim et al., 2024; Solgi et al., 2021; Wu et al., 2025), contaminant source identification (Luo et al., 2025; Mo et al., 2019; Xu et al., 2025), and aquifer parameter inversion (Chen et al., 2025; Wang et al., 2025a; Zhan et al., 2023). However, surrogate modelling for complex biogeochemical kinetic reaction systems remains virtually unexplored.



65 These reaction networks exhibit thermodynamically ordered pathways, sharp redox fronts, and tightly coupled pH-pe  
feedbacks, leading to stiff and highly nonlinear dynamics that conventional neural networks struggle to emulate (Koehn et al.,  
2021). Existing ML surrogates are generally black-box function approximators that do not enforce mass balance, inhibition  
effects, or reaction ordering (McGovern et al., 2019; Sturm and Wexler, 2022), causing error accumulation and instability  
during temporal rollout (Keller and Evans, 2019; Silva et al., 2025). This opaqueness undermines user trust and has prompted  
70 calls to develop inherently interpretable or physics-informed models instead of relying on completely opaque black-box  
approaches (Jiang et al., 2020; Rudin, 2019). As a result, despite progress in ML-accelerated hydrogeochemical modelling,  
there is still a lack of physically consistent and interpretable AI frameworks capable of handling full multi-pathway reaction  
networks.

To overcome these limitations, we turn to graph neural network (GNN). Nowadays, GNN have been extensively applied to  
75 molecular property prediction (Reiser et al., 2022), material screening (Zeng et al., 2022), catalysis modelling (Wang et al.,  
2025b), and has already proven its accuracy and practicality (Reiser et al., 2022; Midlagajni and Rothkopf, 2025). Since  
biogeochemical kinetic reactions inherently involve complex networks of chemical species and their interactions, these  
networks naturally resemble graph structures, where chemical species can be treated as nodes and reactions as edges or  
functional relationships. This structural analogy allows GNNs to inherently capture sequential, branched, and competitive  
80 reaction pathways. Moreover, GNNs offer architectural flexibility, they are not limited to fixed input shapes or predefined  
topologies, making them ideal for modelling systems with variable reaction networks. Studies have shown that trained GNNs  
generalize well across unseen graph structures or chemical mechanisms (Midlagajni and Rothkopf, 2025; Pang et al., 2024;  
Wu et al., 2025). Additionally, node and edge features in a GNN can directly encode domain knowledge (such as concentrations,  
reaction rates and environmental factors) making it possible to embed physical constraints and mechanistic understanding into  
85 the learning process. These strengths make GNNs not only a theoretically appealing but also a practically powerful choice for  
surrogate modelling of biogeochemical reaction systems.

Based on these advantages, we propose PHYGNET (Physically GNN Network), a GNN-based framework that pioneers a  
physics-AI surrogate for microbially-mediated kinetic reaction systems by combining accuracy, efficiency, and physical  
consistency. This structure mirrors the topology of the underlying reaction network, allowing flexible adaptation to varying  
90 microbially-mediated kinetic regimes. A kinetic physics layer enforces mechanistic consistency and mass conservation with  
negligible computation time, while a final MLP layer corrects residuals. To achieve full reactive solute transport ability,  
PHYGNET is integrated into the CPqPy (a COMSOL-PHREEQC coupled Python framework) (Wei and Cao, 2022) as a  
surrogate for PHREEQC. This integration enables direct simulation of coupled transport and reaction. Benchmark comparisons  
against the original CPqPy framework show that PHYGNET reproduces concentration, pH, and pe dynamics with high fidelity,  
95 confirming its reliability and applicability to complex biogeochemical systems.



## 2 Methodology

The PHYGNET framework is developed as a modular architecture designed to emulate complex, microbially-mediated biogeochemical reaction networks. PHYGNET establishes a new mapping protocol that translates the stoichiometry and kinetic logic of given biogeochemical system into a physically integrated graph neural network. By leveraging the inherent structural analogy between biogeochemical pathways and directed graphs, the framework allows for the integration of reaction topologies, ranging from sequential electron-acceptor competition to complex, multi-species metabolic chains.

To demonstrate the framework's capabilities and validate its generalizability, this study utilizes two distinct and highly representative biogeochemical reaction networks: the thermodynamically ordered sequential degradation of toluene (a primary BTEX contaminant) and the chain reductive dechlorination of perchloroethylene (PCE). These systems encompass stiff nonlinearities, multi-electron-acceptor competition, and intricate inhibitory feedbacks among intermediate products (e.g., the well-documented "VC stall"). This dual-validation approach provides strong evidence for its ready extensibility to other critical subsurface processes, such as microbially induced heavy metal reduction (e.g., U(VI) or Cr(VI) bioremediation) and nutrient cycling.

To rigorously test the limits of the PHYGNET framework, we move beyond simple porous media and apply it to a fractured aquifer system. The distinct flow channels and sharp gradients in fractured media (Hyman et al., 2017; Hyman and Jimenez-Martinez, 2018) provide a demanding environment for evaluating the model's stability and accuracy. In this section, we firstly introduce the numerical modelling of groundwater flow and solute transport. Next, we detail the mathematical formulations of the chemical reaction networks. Lastly, the components of PHYGNET will be introduced, including its detailed mathematical modelling and how it can be coupled with COMSOL to accomplish full reactive transport modelling (RTM).

### 2.1 Mathematical Modelling of Flow and Solute Transport in Fractured Media

The numerical simulation is conducted in a 2D rectangular domain measuring 0.5 m × 0.4 m. The domain represents a fractured porous medium where the rock matrix is treated as a continuum and fractures are explicitly represented using a Discrete Fracture Network (DFN) approach. We assume unsteady groundwater and solute transport in a pressurized, isotropic, fractured aquifer. We denote the 2D domain as  $\Omega \in R^2$  with the boundary  $\Gamma$ , in which the union of all fractures is denoted as  $\Omega_f$  and the surrounding rock matrix as  $\Omega_m$ . A conventional subscription m and f are adopted to denote the variables corresponding to the matrix and the fractures, respectively. Within  $\Omega_m$ , the mass balance equation and the constitutive law are:

$$\begin{aligned} \frac{\partial}{\partial t}(\varepsilon_p \rho) + \nabla \cdot (\rho q_m) &= Q, \\ q_m &= -\frac{K_m}{\mu} \nabla p, \end{aligned} \quad (1)$$

Similarly, within the  $\Omega_f$



$$d_f \frac{\partial}{\partial t} (\varepsilon_p \rho) + \nabla_{\tau} \cdot (d_f \rho q_f) = d_f Q, \quad (2)$$

$$q_f = -\frac{K_f}{\mu} \nabla_{\tau} p,$$

125 where  $q_m$  and  $q_f$  are the Darcy flux in  $\Omega_m$  and  $\Omega_f$  respectively,  $p$  is the aqueous pressure,  $\varepsilon_p$  is the porosity,  $\rho$  is the density of water,  $Q$  is the external sources,  $d_f$  is the fracture aperture,  $K_m$  and  $K_f$  are the permeability of  $\Omega_m$  and  $\Omega_f$  respectively, within the  $\Omega_f$ ,  $\nabla_{\tau}$  denotes the tangential direction along the fracture, indicating that the flow and pressure gradient are restricted to the one-dimensional fracture line within this two-dimensional model.  $K_f$  follows the cubic law.

For the solute transport model, we consider only advection and hydrodynamic dispersion, while the reaction terms (S) which  
130 handled by the PHYGNET are solved separately. Thus, the governing equation of solute transport in  $\Omega_m$  can be expressed as:

$$\frac{\partial \varepsilon_p C}{\partial t} + \nabla \cdot J + q_m \cdot \nabla C = S, \quad (3)$$

$$J = -D \nabla C,$$

Similarly, within the  $\Omega_f$

$$d_f \left( \frac{\partial \varepsilon_p C}{\partial t} + \nabla_{\tau} \cdot J + q_f \cdot \nabla_{\tau} C \right) = d_f S + n_0, \quad (4)$$

$$J = -D \nabla_{\tau} C,$$

where  $C$  is the concentration of solute,  $t$  demotes time,  $J$  is the hydrodynamic dispersion flux,  $S$  is the solute source/sink term,  
135  $n_0$  is initial solute amount in the fracture system,  $D$  is the hydrodynamic dispersion coefficient.

## 2.2 Mathematical Formulations of Kinetic Reaction Networks

In natural subsurface environments, microbially-driven biogeochemical transformations rarely occur as isolated, single-step processes. Instead, they manifest as complex, interconnected kinetic reaction networks. Whether modelling the thermodynamically ordered oxidation of hydrocarbons or the sequential reductive dechlorination of chlorinated solvents, the  
140 underlying mathematical architecture of these metabolic pathways shares a universal structure.

Consider a generalized biogeochemical reaction step  $j$  within a complex network, which can be conceptually represented by the following stoichiometry:



where  $A$  represents the primary substrate (e.g., a contaminant),  $B$  represents an electron acceptor or donor,  $C$  and  $D$  are the  
145 resulting products, and  $v$  the corresponding stoichiometric coefficients,  $r_j(\mathbf{C}, \mathbf{E})$  is the kinetic rate of reaction  $j$ . This reaction rate is inherently a highly nonlinear function dependent on the concentration vector of all involved species ( $\mathbf{C}$ ) and the localized environmental state variables ( $\mathbf{E}$ ), such as pH, pe.

Mathematically, the temporal evolution of any chemical species  $i$  within a localized batch system (i.e., the reaction step in an operator-splitting RTM framework) is governed by a system of stiff, coupled ordinary differential equations (ODEs):



150

$$\frac{dC_i}{dt} = \sum_{j=1}^M \pm v_{i,j} r_j(\mathbf{C}, \mathbf{E}) \quad (6)$$

where  $C_i$  is the concentration of species  $i$ ,  $t$  is the time,  $M$  is the total number of reactions in the network,  $v_{i,j}$  represents the stoichiometric coefficient of species  $i$  in reaction  $j$  (positive for products, negative for reactants).

The crux of the numerical complexity lies in the generalized kinetic rate,  $r_j$ . To capture the intricate biogeochemical dependencies,  $r_j$  is typically formulated as a multiplicative combination of a maximum rate capacity, substrate limitations, and network-level regulatory feedbacks. A generalized multi-Monod kinetic formulation can be expressed as:

$$r_j = k_{max,j} \cdot \left( \frac{C_A}{K_A + C_A} \right) \cdot \left( \frac{C_B}{K_B + C_B} \right) \cdot I_j(\mathbf{C}) \quad (7)$$

where  $k_{max,j}$  is the maximum specific reaction rate (reflecting maximum specific microbial growth and biomass yield) under optimal environmental conditions ( $\mathbf{E}$ ). The fractional terms (e.g.,  $\frac{C_A}{K_A + C_A}$ ) are Monod expressions representing thermodynamic or enzymatic limitations, where  $K_i$  is the half-saturation constant of species  $i$ . These terms drive the reaction forward when substrates are abundant but choke it as concentrations approach zero.  $I_j(\mathbf{C})$  encapsulates the intricate inhibitory feedbacks from the surrounding chemical network.

In complex systems, the inhibition term  $I_j(\mathbf{C})$  acts as a regulatory gate. It is frequently modelled using competitive or non-competitive enzymatic inhibition functions, generalized as:

$$I_j(\mathbf{C}) = \prod_{x \in X_j} \frac{K_{I,x}}{K_{I,x} + C_x} \quad (8)$$

where  $X_j$  is the set of all species that inhibit reaction  $j$ ,  $C_x$  is the concentration of the inhibiting species, and  $K_{I,x}$  is the inhibition threshold constant. This explicit mathematical term elegantly captures critical subsurface phenomena. For example, the presence of a thermodynamically more favourable electron acceptor ( $C_x$ ) will suppress secondary metabolic pathways, or the accumulation of a toxic intermediate product will stall the downstream degradation chain.

The highly coupled nature of Eq. (6) to Eq. (8), combined with feedback loops that can fluctuate over several orders of magnitude, results in severe numerical stiffness. Solving this generalized ODE system iteratively at every spatial grid cell using traditional Newton-Raphson methods imposes an overwhelming computational burden.

However, the inherent architecture of this generalized formulation exhibits a profound structural analogy to a directed graph. The discrete chemical species ( $A, B, C, D$ ) serve as nodes, the stoichiometric transformations ( $v$ ) form directed edges representing mass flow, and the inhibition terms ( $I_j$ ) act as regulatory signals passed between specific nodes. This new topological mapping provides the foundational rationale for the PHYGNET framework, allowing the model to accelerate simulation efficiency by directly learning the message-passing dynamics of these structured biological networks.

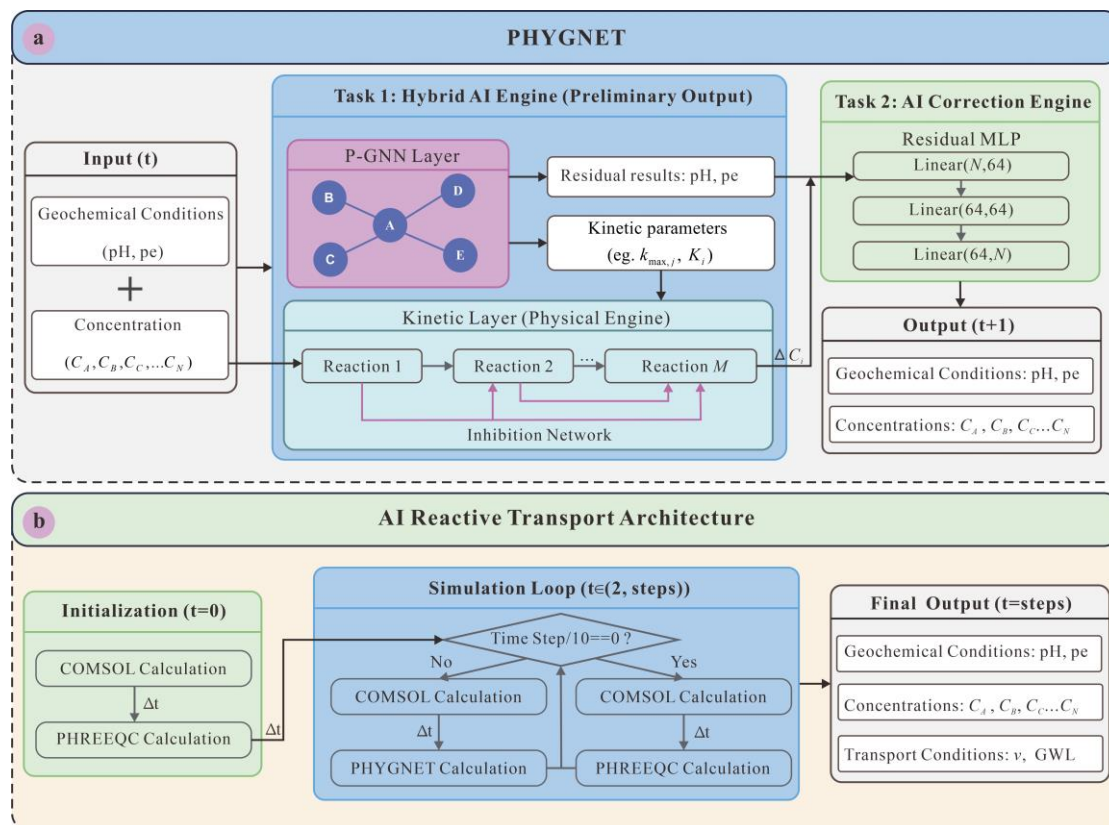


## 2.3 Physically Integrated Surrogate GNN for Reactive Process

### 2.3.1 Framework Overview

Building upon the formal definition of the sequential kinetic pathways and their corresponding governing equations, we now proceed to the structural realization of the PHYGNET framework. Having clarified the mechanistic dependencies of the biochemical system, this stage involves translating these established relationships into a parametric graph architecture. By mapping the previously defined stoichiometry and inhibitory feedbacks into a directed graph topology, the model transitions from theoretical description to an active surrogate capable of emulating complex biogeochemical reaction-transport dynamics with high fidelity.

PHYGNET consists of three components: a parametric GNN (P-GNN), a Monod-based kinetic physics layer, and a residual corrector (see Fig. 1a). The P-GNN encodes each biogeochemical system as a directed graph, where nodes represent chemical species and reaction pathways, and edges capture reactant flows and inhibitory relationships. Node features include log-transformed concentrations. Through message passing, the network learns latent embeddings and predicts biological kinetic parameters ( $k_{max,j}$  are predicted in this paper) for each pathway. Following the P-GNN, we integrate an explicit kinetic physics layer to ensure fundamental mass conservation and stoichiometric consistency. This addition prevents the “unphysical drift” commonly associated with pure data-driven surrogates with negligible computational cost, as the direct evaluation of kinetic rate laws is significantly faster than the iterative convergence required in traditional solvers. Finally, a lightweight multilayer perceptron (MLP) refines the outputs (concentrations, pH, and pe) by correcting residual errors. This decoupled residual block preserves interpretability while improving accuracy across tasks.



195

**Figure 1: Overview of the PHYGNET framework and its integration into AI-accelerated RTMs. (a) PHYGNET combines a P-GNN for reaction rate estimation, a Monod-based kinetic layer, and a residual MLP for correction. (b) In the AI RTM architecture, PHYGNET serves as a surrogate for PHREEQC between periodic full-physics recalibrations.**

To balance physical consistency with predictive accuracy, PHYGNET adopts a multi-task learning strategy that simultaneously captures chemical dynamics and system states. Specifically, the model is trained to jointly predict species concentrations, pH, pe, and the kinetic parameters using a unified loss function. This formulation enables shared latent representations that integrate fine-scale reactivity with global geochemical behaviour. Although kinetic parameters are not explicitly labelled, the model infers them implicitly through patterns in concentration and condition inputs. SHAP-based analysis confirms that the learned rate controls are both plausible and interpretable, with higher reactant concentrations often linked to elevated reaction potential.

### 205 2.3.2 Detailed Mathematical Formulation of P-GNN

P-GNN is built on Graph Attention Network (GAT) layers. In a GAT layer each node's features are linearly transformed and then self-attention is used to weight contributions from neighbouring nodes. Specifically, for node  $i$  with feature vector  $h_i$ , we compute an attention score for each neighbour  $j \in N(i)$  as

$$e_{ij} = a^T [Wh_i \parallel Wh_j] \quad (9)$$



210 where  $W$  is a shared weight matrix,  $a$  is an attention vector, and “||” denotes concatenation. These scores are normalized by a softmax over  $j$  to give attention coefficients.

$$\alpha_{ij} = \frac{\exp(e_{ij})}{\sum_{k \in \mathcal{N}(i)} \exp(e_{ik})} \quad (10)$$

The node’s new feature is then a weighted sum of its neighbors:

$$h'_i = \sigma \left( \sum_{j \in \mathcal{N}(i)} \alpha_{ij} W h_j \right) \quad (11)$$

215 where  $\sigma$  is a nonlinearity (LeakyReLU). Multi-head attention is typically used: independent attention mechanisms compute features which are concatenated (or averaged in the final layer) to stabilize learning (Veličković et al., 2018). Here we use 4, 2, 1 in three GAT layers respectively.

P-GNN applies 3 stacked GAT layers to this heterogeneous graph. At each layer, every node (species or reaction) receives messages from its incoming neighbours weighted by attention as above. Through this message-passing, species nodes gather information from the reactions they participate in and vice versa. After 3 layers, each reaction node has an embedding  $h_i^{(L)}$  that aggregates contextual information from all connected species (and higher-order connections). A final readout or MLP head is applied to each reaction node’s embedding to predict kinetic parameters. Similarly, global environment outputs (pH and pe corrections) are produced by aggregating over relevant nodes. All predictions are derived from the learned embeddings, attention weights focus on critical species-reaction interactions, and each predicted rate is a function of the learned subgraph pattern around that reaction. In effect, the GAT layers perform relational reasoning over the chemical graph, with updates governed by equations like those above.

225

### 2.3.3 Encoding P-GNN into PHYGNET

While the P-GNN effectively captures the topological dependencies and predicts dynamic reaction constraints (e.g.,  $k_{max,j}$ ) based on message-passing algorithms, these purely data-driven outputs must be physically anchored. The core innovation of the framework lies in encoding the P-GNN within the broader PHYGNET architecture through a differentiable, hard-coded physics layer. This layer serves as a deterministic bridge between the abstract latent embeddings and the strict mass conservation laws governing hydrogeochemical systems.

230

Instead of allowing the neural network to directly predict future concentrations, which is a common pitfall in naive deep learning surrogates that inevitably leads to mass balance violations, PHYGNET restricts the P-GNN to predicting only the localized kinetic parameters. These dynamically predicted parameters are injected into the differentiable kinetics layer, which explicitly executes the multi-Monod rate laws, inhibition functions, and stoichiometric mass balances formulated in Equations (6) to (8). By utilizing differentiable tensor operations, the layer calculates the exact mass of substrates consumed and intermediate products generated over the temporal step  $\Delta t$ .

235



240 This specific encoding strategy guarantees that regardless of the specific biogeochemical reaction network being modelled, whether involving the parallel thermodynamic competition of electron acceptors (as seen in BTEX oxidation) or the sequential, inhibitory chain reactions of chlorinated solvents (such as PCE dechlorination), elemental mass is strictly conserved. The generalized stoichiometric matrix ( $v_{i,j}$ ) acts as an immutable physical inductive bias within the network.

245 Furthermore, real-world hydrogeochemical systems often exhibit subtle, unmodeled thermodynamic fluctuations. To account for these subtleties without over-complicating the hard-coded physics layer, the physics-constrained concentration estimates are concatenated with the updated environmental features and passed through a shallow Multi-Layer Perceptron (MLP) corrector. This residual architecture ensures that the final predicted state maintains strict primary mass balance while possessing the flexibility to capture complex environmental feedbacks.

250 Ultimately, this encoding paradigm ensures that during end-to-end training, the gradients computed from the final loss function flow backward through the immutable physics layer and into the P-GNN. This forces the graph network to continuously adjust its internal weights until it learns the true underlying biogeochemical dynamics, rather than merely memorizing statistical mappings.

## 2.4 Coupling PHYGNET with COMSOL

255 To demonstrate the surrogate model's capability in dynamic flow systems, we integrated PHYGNET into the CPqPy framework (see Fig. b). CPqPy originally couples COMSOL Multiphysics and PHREEQC through operator splitting, solving solute transport and reaction in alternating steps (Wei and Cao, 2022). We retained this architecture while substituting PHREEQC with PHYGNET for most time steps, and renamed it as CPgPy. Specifically, each time step begins with a solute transport simulation in COMSOL, from which nodal concentrations are extracted and passed to PHYGNET. These inputs (species concentrations, pH, and pe) are used to construct a batched reaction graph, which is then processed by PHYGNET to predict updated concentrations and environmental parameters. The predictions are converted back to COMSOL-readable 260 formats and used to initialize the next transport step.

To prevent long-term drift and error accumulation, we adopt a hybrid strategy: every 10 simulation time steps, the framework calls PHREEQC to perform full geochemical simulation using the original kinetic definitions. This periodic correction stabilizes redox-sensitive parameters such as pH and pe, and helps recalibrate species interactions in the absence of explicit rate supervision. The input files for PHREEQC are automatically generated based on the latest COMSOL outputs and include 265 both solution conditions and dynamic reaction rates, while the outputs are parsed back into the pipeline. This design ensures physical fidelity without sacrificing computational speed.

All modules are synchronized via a standardized file interface, ensuring compatibility with COMSOL's external input/output protocol. The entire system is controlled via Python, with MATLAB scripts used to initiate COMSOL simulations and restart services at each iteration for robustness. Through this integration, the PHYGNET-enabled CPgPy framework achieves efficient, 270 modular simulation of reactive solute transport while preserving physical interpretability and model generalizability.



### 3 Application

To systematically evaluate the universal mapping capability and the physical fidelity of the PHYGNET framework, we establish two benchmark networks. These networks represent two of the most ubiquitous yet mathematically challenging biogeochemical kinetic systems in subsurface environments: thermodynamically ordered competitive oxidation (Case A) and sequential chain reductive dichlorination (Case B). By validating the surrogate against both systems, we ensure that PHYGNET's underlying topology mapping can accommodate fundamentally different biogeochemical architectures without structural modification.

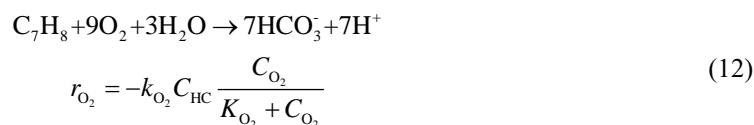
#### 3.1 Biogeochemical Kinetic Networks Setup

##### 3.1.1 Case A: Competitive Degradation of BTEX

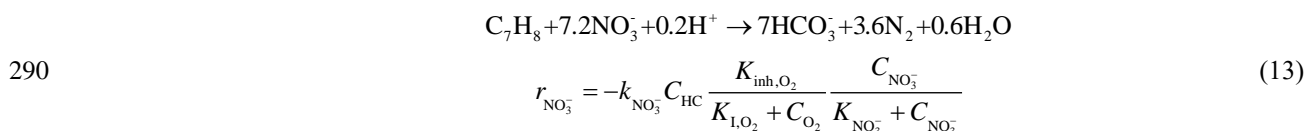
The first benchmark focuses on the aerobic and anaerobic oxidation of toluene (a representative BTEX compound), which involves multiple electron acceptors competing in a strict thermodynamic sequence. As groundwater transports the hydrocarbon plume, indigenous microbes preferentially utilize electron acceptors that yield the highest free energy. When dissolved oxygen  $O_2$  is depleted, the system sequentially shifts to nitrate ( $NO_3^-$ ), and subsequently to sulfate ( $SO_4^{2-}$ ), ultimately leading to methanogenesis.

This system is mathematically formulated using multiplicative Monod kinetics, incorporating competitive and non-competitive inhibitory functions to enforce the thermodynamic hierarchy. The reaction network is conceptualized as follows:

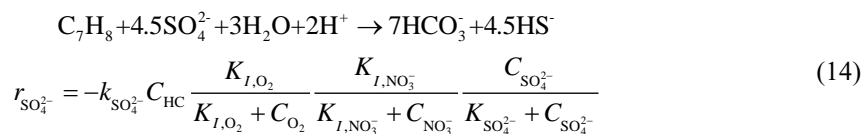
(1) Aerobic Respiration:



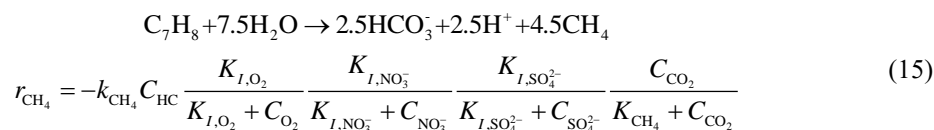
(2) Nitrate Reduction (Denitrification):



(3) Sulfate Reduction:



(4) Methanogenesis:



295 The crucial numerical challenge here lies in the inhibition terms (e.g.,  $\frac{K_{I,O_2}}{K_{I,O_2} + C_{O_2}}$ ). These terms act as mathematical “switches”

that suddenly activate or deactivate secondary reactions as the primary electron acceptor concentration approaches zero, creating sharp spatial and temporal gradients (stiffness) that are notoriously difficult for traditional solvers to integrate efficiently.

### 3.1.2 Case B: Sequential Reductive Dechlorination of PCE

300 To further test the framework’s capability to capture chain reactions and intermediate product toxicity, we introduce the sequential reductive dechlorination of perchloroethylene (PCE) as the second benchmark. In highly reducing environments, specialized microbes (e.g., dehalococcoides) strip chlorine atoms from the solvent molecule, substituting them with hydrogen. The pathway proceeds stepwise from PCE to trichloroethylene (TCE), dichloroethylene (DCE), vinyl chloride (VC), and finally to benign ethene, accompanied by the continuous release of chloride ions (Cl<sup>-</sup>).

305 Unlike the parallel competition in Case A, this system is characterized by sequential mass flow and profound cross-species inhibition. High concentrations of parent compounds (PCE and TCE) are known to strongly inhibit the degradation of downstream intermediates, a phenomenon that frequently leads to the dangerous accumulation of VC (a known carcinogen), often referred to as “VC stall”.

The mathematical formulation for this chain reaction utilizes multi-Monod kinetics with competitive inhibition terms. For 310 instance, the degradation rate of DCE is suppressed by both PCE and TCE, while the degradation of VC is heavily suppressed by TCE and DCE. The generalized rate for a specific step (e.g., the degradation of component X to Y) is defined as:

$$X \rightarrow Y + Cl^-$$

$$r_X = k_{max,X} \cdot \left( \frac{C_X}{K_X + C_X} \right) \cdot \prod_{i \in P_X} \left( \frac{K_{I,i}}{K_{I,i} + C_i} \right) \quad (16)$$

where  $P_X$  denotes the set of parent/inhibitory compounds affecting step  $X$ , and  $K_{I,i}$  is the competitive inhibition constant for compound  $i$ .

315 This specific kinetic structure forces the solver to track mass across multiple tightly coupled species. Even a minute error in predicting the early PCE dechlorination rate will exponentially propagate down the chain, completely distorting the predicted VC and ethene concentrations. Therefore, this benchmark serves as an ultimate test for PHYGNET’s differentiable physics layer, proving whether it can strictly enforce mass conservation across a multi-stage sequential pathway while correctly learning the complex interplay of downstream inhibitory signals.



## 320 3.2 Data Generation and Training Process

### 3.2.1 State Space Sampling and Ground Truth Simulation

To ensure the PHYGNET surrogate is robust and universally applicable across a highly heterogeneous macroscopic domain, the model must be trained on a comprehensive dataset that thoroughly explores the biogeochemical state space. Relying on a limited set of initial conditions often leads to severe out-of-distribution (OOD) errors when the surrogate encounters sharp concentration gradients or depleted zones during full reactive transport coupling. Therefore, we employed a systematic data generation and pre-processing pipeline applicable to both kinetic benchmarks.

We utilized Latin Hypercube Sampling (LHS) to efficiently sample the multi-dimensional parameter space, generating thousands of distinct initial state vectors ( $\mathbf{C}_0, \mathbf{E}_0$ ). For Case A (BTEX), The sampled space included independent log-uniform distributions for HC, O<sub>2</sub>, NO<sub>3</sub><sup>-</sup>, SO<sub>4</sub><sup>2-</sup>, and CH<sub>4</sub>, ensuring the model experiences scenarios ranging from fully aerobic to strictly methanogenic conditions. For Case B (PCE), The sampling space also explicitly covered a wide spectrum of parent (PCE, TCE) and daughter (DCE, VC, ethene) product combinations. This deliberately included “bottleneck” scenarios (such as high PCE/TCE concentrations coexisting with trace VC) to compel the model to learn the critical “VC stall” inhibitory dynamics. For each sampled initial state, a localized batch simulation was executed using the standard geochemical code PHREEQC. The solver was configured to strictly integrate the stiff ordinary differential equations defined in Section 3.1 over a designated simulation period. To mimic the discrete time-stepping inherent to the Operator-Splitting (OS) transport framework, the continuous concentration profiles were extracted at fixed intervals ( $\Delta t$ ), producing paired input-output training tensors:  $\{(\mathbf{C}_t, \mathbf{E}_t) \rightarrow (\mathbf{C}_{t+\Delta t}, \mathbf{E}_{t+\Delta t})\}$ . In total, about 50,000 discrete state transitions were generated for each benchmark system.

### 3.2.2 Data Transformation and Training Strategy

To map the tabular batch data into the graph-based format required by PHYGNET, the chemical species and reaction steps were encoded as node features within the topological structures defined in Fig. 1.

A critical pre-processing step in biogeochemical machine learning involves addressing the vast disparity in concentration scales. Contaminant concentrations can span more than ten orders of magnitude (e.g., from 10<sup>-3</sup> mol/L near a source zone to 10<sup>-12</sup> mol/L at the plume fringe). Feeding raw linear concentrations into a neural network typically causes vanishing gradients for trace species. To mitigate this, all species concentrations were transformed using a regularized natural logarithm:

$$345 \quad C'_i = \frac{\ln(\max(C_i, 0) + \varepsilon) - \mu_i}{\sigma_i} \quad (17)$$

where  $\varepsilon$  is a conservatively small threshold (e.g., 10<sup>-12</sup> mol/L) representing the physical non-detect limit, and  $\mu_i$  and  $\sigma_i$  are the mean and standard deviation of the log-transformed training set. Environmental state variables (pH, pe) were standardized using standard linear z-score normalization.

To strictly enforce the physics-informed inductive bias while allowing for minor thermodynamic flexibility, PHYGNET is trained end-to-end using a dual-task objective function.



Task 1 (Physics Constraint): Evaluates the discrepancy between the purely physics-constrained predictions (output solely from the differentiable kinetics layer based on P-GNN's predicted  $k_{\max}$ ) and the ground truth.

Task 2 (Residual Correction): Evaluates the discrepancy of the final predictions after the residual MLP corrector has applied minor thermodynamic fine-tuning.

355 Given the sequential nature of subsurface kinetics, a standard Mean Squared Error (MSE) loss often disproportionately favors accurately predicting high-concentration parent compounds, largely ignoring trace intermediate products. To compel the network to learn the intricate inhibitory dynamics of trace by-products (e.g., VC and ethene), we employed a species-weighted Smooth L1 Loss (Huber Loss) function. The total loss  $L_{\text{total}}$  is formulated as:

$$L_{\text{Task}} = \sum_{i \in \mathcal{V}_{\text{species}}} \omega_i \cdot \text{SmoothL1}(C'_{i,\text{pred}}, C'_{i,\text{true}}) + \sum_{k \in \{pH, pe\}} \text{SmoothL1}(E_{k,\text{pred}}, E_{k,\text{true}}) \quad (18)$$

$$L_{\text{total}} = L_{\text{Task1}} + L_{\text{Task2}}$$

360 where  $\omega_i$  is a manually assigned species-specific weight vector. In our code implementation, higher weights were explicitly assigned to downstream daughter products to penalize sequential error propagation. Both tasks are optimized simultaneously, ensuring that the gradients flowing backward from  $L_{\text{Task1}}$  strictly force the P-GNN to learn the true physical rate constants rather than relying entirely on the MLP corrector.

The framework was implemented using PyTorch Geometric and trained on an NVIDIA GPU using the Adam optimizer (initial 365 learning rate of  $10^{-3}$ ). An early stopping mechanism was deployed with a patience of 20 epochs to prevent overfitting. Fig. 2 shows that the total loss and its components steadily decrease over training epochs, demonstrating both data fitting and physical regularization.

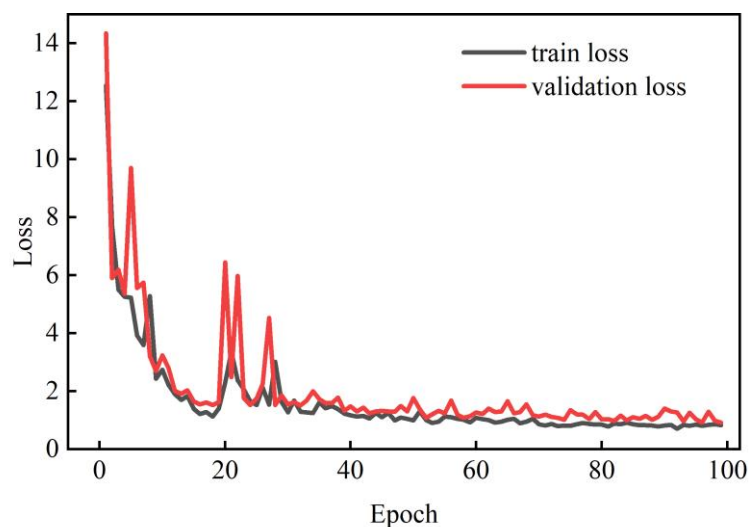
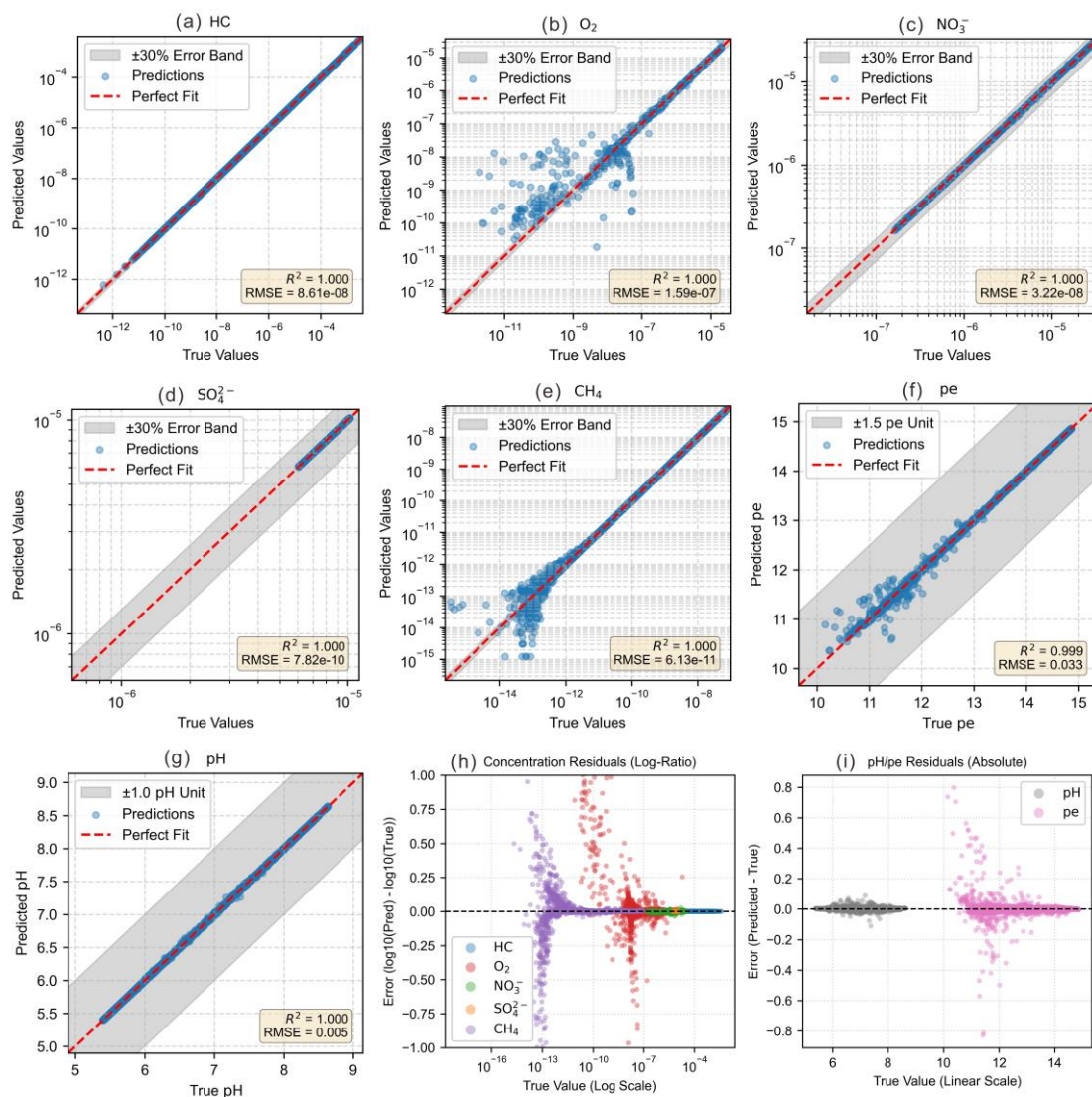


Figure 2: The total loss curves of training and validation (Case A).



### 370 3.3 Model Performance

To apply PHYGNET to RTMs, the first step should be to ensure that PHYGNET itself achieves sufficiently accurate simulation results. This will minimize errors arising from reactive solute transport modelling. We evaluate the predictive performance of PHYGNET across two distinct kinetic networks: the competitive degradation of BTEX (Case A) and the sequential reductive dechlorination of PCE (Case B). The evaluation encompasses all output targets, including primary substrates, competing  
 375 electron acceptors, intermediate daughter products, and geochemical conditions (pH, pe).



**Figure 3: Predictive performance of PHYGNET for Case A.** Scatter plots compare PHYGNET predictions and true values for five solute species (HC, O<sub>2</sub>, NO<sub>3</sub><sup>-</sup>, SO<sub>4</sub><sup>2-</sup>, CH<sub>4</sub>) and two geochemical indicators (pH and pe). Lower-middle and lower-right panels show residual analysis for concentrations (log-ratio) and pH/pe (absolute error).

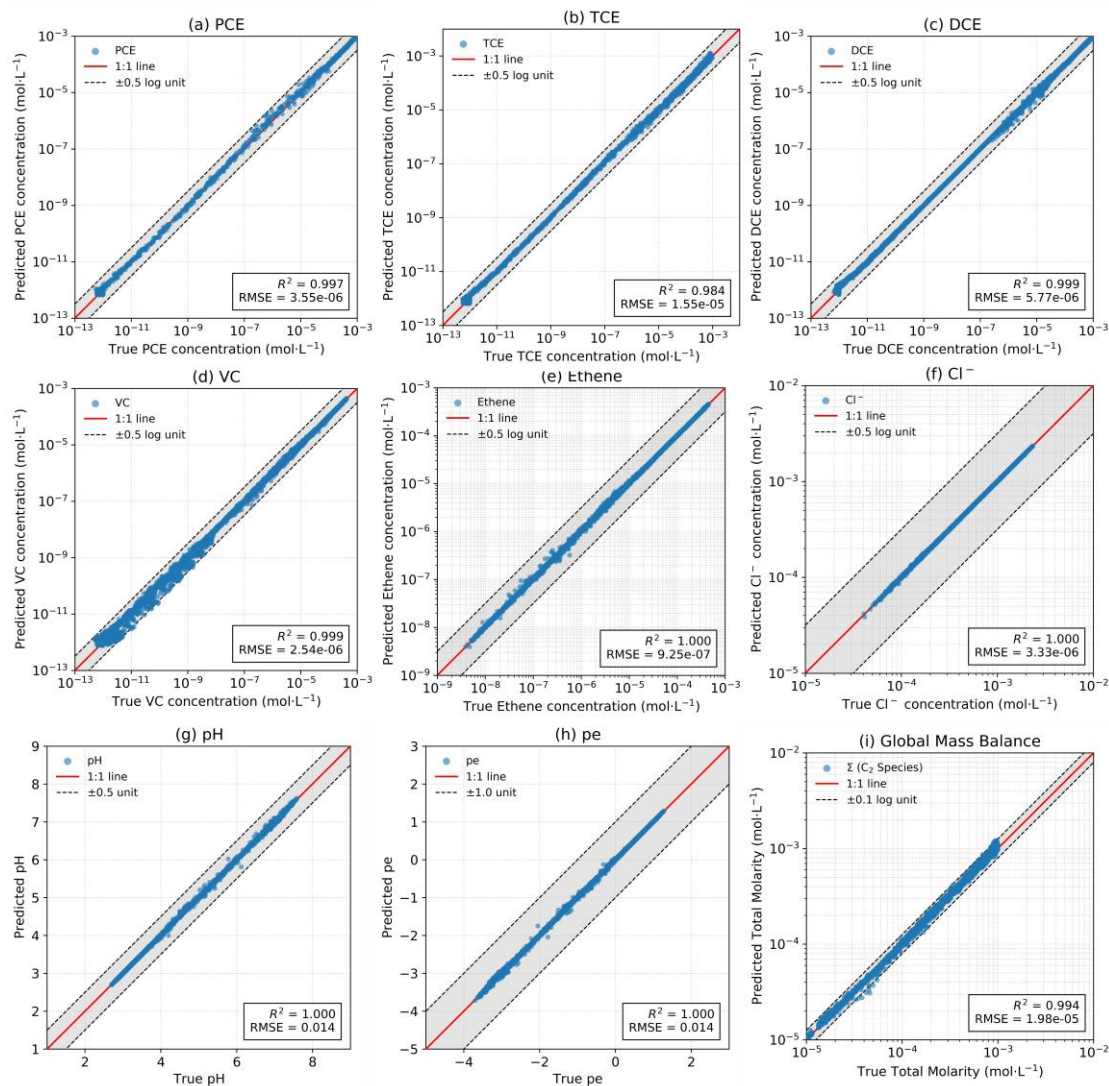


**Figure 4: Predictive performance of PHYGNET for Case B. Panels (a-h) display the predictions for parent solvents, intermediate daughter products, and environmental variables. Panel (i) validates the global mass balance of  $C_2$  backbone species ( $\Sigma$ PCE, TCE, DCE, VC, Ethene). The predicted total molarity perfectly aligns with the ground truth within a highly stringent  $\pm 0.1$  log unit error band, confirming the rigorous mass conservation enforced by the internal physics layer.**

385

Across all targets, PHYGNET achieves near-perfect agreement with ground truth values, reflected by  $R^2$  scores above 0.98 and minimal root mean square errors (RMSE). For the BTEX system (Case A), key species like HC and  $NO_3^-$  exhibit near-zero deviation across all concentration regimes. Remarkably, the surrogate performs equally well in the PCE system (Case B), accurately capturing the complex, non-linear accumulation and decay dynamics of intermediate products like DCE and VC.

390 The predictions for geochemical indicators (pH and pe) in both cases are also highly accurate; for instance, over 98% of predictions fall well within  $\pm 0.5$  pH units and  $\pm 1.0$  pe units. These results validate PHYGNET's ability to simultaneously resolve fast-reacting organic species and slow-evolving redox environments without violating elemental mass balances.



To further probe the residual structure, we examined the log-ratio residuals for concentrations and absolute errors for pH/pe. While the overall fidelity is exceptionally high, the largest relative uncertainties emerge predominantly in O<sub>2</sub> and CH<sub>4</sub> (for Case A), and trace levels of VC or Ethene (for Case B). These minor deviations stem from two primary physical and numerical causes:

1. Scale sensitivity at detection limits: These specific species often exist near physical non-detect limits (e.g., 10<sup>-15</sup> to 10<sup>-10</sup> mol/L). In this extreme low-concentration regime, even infinitesimally small absolute errors will translate into large log-scale variances on the parity plots.
2. Network hierarchy and error propagation: In Case A, the concentrations of CH<sub>4</sub> is heavily influenced by upstream electron acceptors. The model must learn the implicit competition among O<sub>2</sub>, NO<sub>3</sub><sup>-</sup>, and SO<sub>4</sub><sup>2-</sup>. Similarly, in Case B, predicting trace VC and Ethene requires the model to correctly resolve the cascaded inhibitory feedbacks from PCE and TCE (the “VC stall” effect). These hierarchical dependencies introduce severe nonlinearities, making downstream trace species inherently more difficult to resolve perfectly than the primary substrates.

Despite these visible log-scale deviations at the lower bounds, the discrepancies are largely confined to values near or below analytical detection thresholds, where numerical dispersion and discretization effects naturally dominate (Hammond et al., 2014). Such errors are ubiquitous in traditional RTMs and are unlikely to affect macroscopic plume interpretation or transport simulation accuracy, as they fall well within the noise level of environmental measurement or numerical approximation (Li et al., 2008). Importantly, PHYGNET retains pristine fidelity across all ecologically and computationally relevant concentration ranges for both competitive and sequential reaction networks.

Crucially, while resolving trace-level intermediate products poses a significant challenge, the PHYGNET framework completely eradicates a fatal flaw of traditional pure data-driven surrogates: the violation of mass conservation. As demonstrated in Fig. 4i, we evaluated the global mass balance of the Case B network by tracking the total molarity of all two-carbon (C<sub>2</sub>) species (ΣPCE, TCE, DCE, VC, Ethene). Because the sequential dechlorination process merely strips chlorine atoms while leaving the C<sub>2</sub> carbon backbone intact, the sum of these species must theoretically remain constant throughout the temporal integration. As Fig. 4i illustrates, the predicted total molarities align perfectly with the 1:1 ground truth line, constrained within an exceptionally tight error margin of ±0.1 log units. This pristine conservation confirms that the hard-coded differentiable kinetics layer is functioning exactly as intended. By serving as an immutable inductive bias, it strictly regulates the stoichiometric mass transfer based on the P-GNN’s predicted reaction rates, preventing the accumulation of non-physical mass errors even when the network is navigating the extreme nonlinearities of the “VC stall”.

#### 4 Discussions

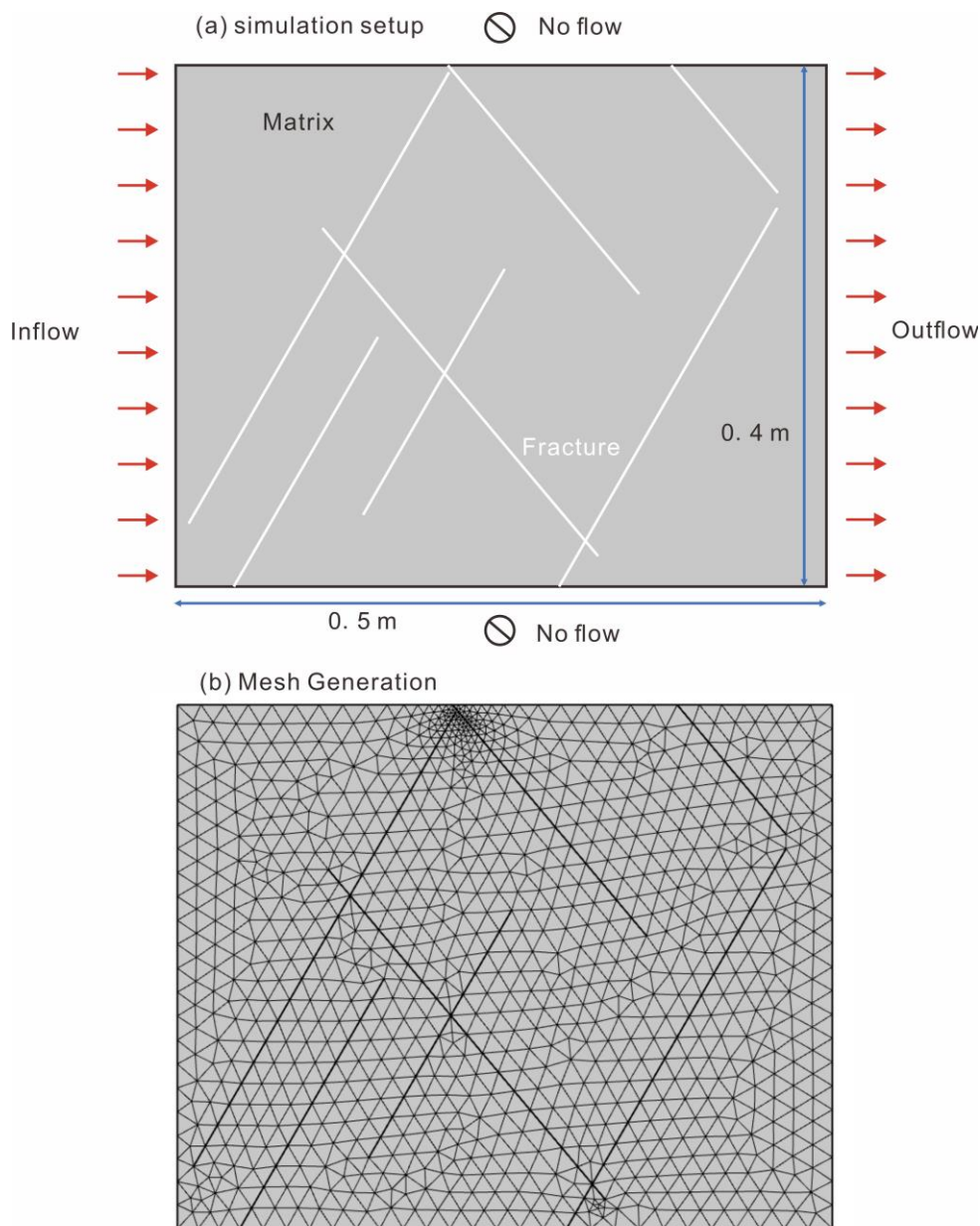
Having successfully validated the surrogate’s high-fidelity emulation and topological generalizability at the batch scale, this section evaluates the PHYGNET framework’s macroscopic utility and internal physical consistency.



425 The subsequent discussion evaluates PHYGNET across three key dimensions: macroscopic RTM performance (Sections 4.1  
and 4.2), computational efficiency (Section 4.3), and model interpretability (Section 4.4). Given that the operator-splitting  
interface is inherently system-agnostic, a single spatial demonstration is mathematically sufficient to validate the framework's  
robustness. Consequently, we focus on the BTEX competitive degradation system (Case A) embedded within a highly  
heterogeneous fractured aquifer. This scenario rigorously tests the surrogate's stability, spatial accuracy, and computational  
acceleration under extreme physical gradients. Furthermore, we apply SHAP (Shapley Additive Explanations) analysis to  
430 confirm that the network autonomously learns the underlying biogeochemical logic, capturing both competitive and sequential-  
inhibitory mechanisms, rather than simply overfitting the training data.

#### 4.1 Setup of the Fractured Aquifer RTM

Specially, we simulate reactive transport within a 2D fractured domain using the CPgPy framework. Establishing validity in  
this highly heterogeneous condition suggests that the framework can readily extend to other subsurface conditions. The  
435 rectangular domain measures  $0.5 \text{ m} \times 0.4 \text{ m}$  and incorporates two intersecting fracture sets: three fractures oriented at  $310^\circ$  and  
three at  $60^\circ$ , respectively. A discrete fracture network (DFN) approach is adopted, with local mesh refinement along fracture  
planes to resolve sharp hydraulic and chemical gradients (see [Fig. 5](#)).



440 **Figure: 5. Schematic of the idealized 2D fractured aquifer domain and mesh generation. (a) Simulation setup: A  $0.5 \text{ m} \times 0.4 \text{ m}$  rectangular domain representing a porous matrix with embedded fractures. Red arrows indicate inflow from the left boundary and outflow from the right boundary; top and bottom boundaries are no-flow conditions. Fractures are depicted as white lines traversing the matrix. (b) Mesh Generation: Unstructured triangular mesh discretizing the domain, with finer resolution near fracture intersections to capture localized gradients in concentration or velocity. Mesh aligns with fracture geometry to ensure accurate representation of flow and reaction processes.**

445 Groundwater flow is driven by given-head boundaries on the left and right edges, establishing a horizontal hydraulic gradient of 0.02 from left to right. The top and bottom boundaries are treated to be no-flow. Solute transport is solved with the advection-



dispersion equation, with flow field solved with a groundwater flow model built into COMSOL. The mesh is generated with refinement around fractures to capture sharp hydraulic gradient (see Fig. 5b)

Initial biogeochemical conditions include a toluene (HC) contamination plume centered near the left boundary, with a peak concentration of  $5 \times 10^{-3}$  mol/L (see Fig. 6a). Background concentrations are set to  $2 \times 10^{-5}$  mol/L ( $O_2$ ),  $3 \times 10^{-5}$  mol/L ( $NO_3^-$ ),  $1 \times 10^{-5}$  mol/L ( $SO_4^{2-}$ ), and 0 mol/L ( $CH_4$ ). The left boundary maintains inflow with fixed background concentrations, while the right acts as an advective outflow. The upper and lower boundaries are impermeable to both groundwater flow and solute transport. Detailed kinetic parameters can be seen in Table 1.

**Table 1. Key hydrogeological and transport parameters used in the reactive transport simulation.**

Parameter	Unit	value
Given hydraulic head (left)	m	1
Given hydraulic head (right)	m	0.99
Matrix Hydraulic conductivity	m/d	1
Fracture aperture	m	0.01
Longitudinal dispersivity	m	0.01
Transverse dispersivity	m	0.001
Matrix porosity	-	0.3
Fracture porosity	-	0.7

The simulation step is 1 hour, for a total of 240 hours in this paper. At each step, species concentrations and hydraulic head fields are exported from COMSOL via MATLAB LiveLink scripts. These outputs serve as inputs to PHYGNET, which predicts the system's chemical evolution. Every 10 steps, CPgPy invokes PHREEQC to recompute full reaction equilibria, ensuring long-term chemical consistency. This hybrid execution scheme balances predictive efficiency with thermodynamic rigor.

#### 4.2 Coupled Reactive Transport Capability of PHYGNET

The spatiotemporal evolution of hydrocarbon (HC) concentration (Fig. 6) demonstrates that PHYGNET successfully participates in the transport process and responds dynamically to flow-driven migration. At early times ( $t = 0-10$  h), the HC plume is primarily confined near the source zone and begins to migrate along preferential flow paths controlled by the fracture network. As time progresses ( $t = 60-120$  h), the plume elongates and spreads, exhibiting clear anisotropic transport behaviour governed by fracture-dominated advection and transverse dispersion. At later stages ( $t = 200-240$  h), the plume morphology stabilizes, with noticeable mass transfer into the surrounding matrix, indicating the onset of diffusion-controlled storage and redistribution.

This continuous evolution from advection-dominated transport to matrix interaction reflects that PHYGNET is not operating as an isolated reaction predictor, but is actively embedded within the transport loop. The model continuously updates concentration fields in response to spatial transport processes, confirming that the coupling between flow, transport, and reaction is effectively maintained.

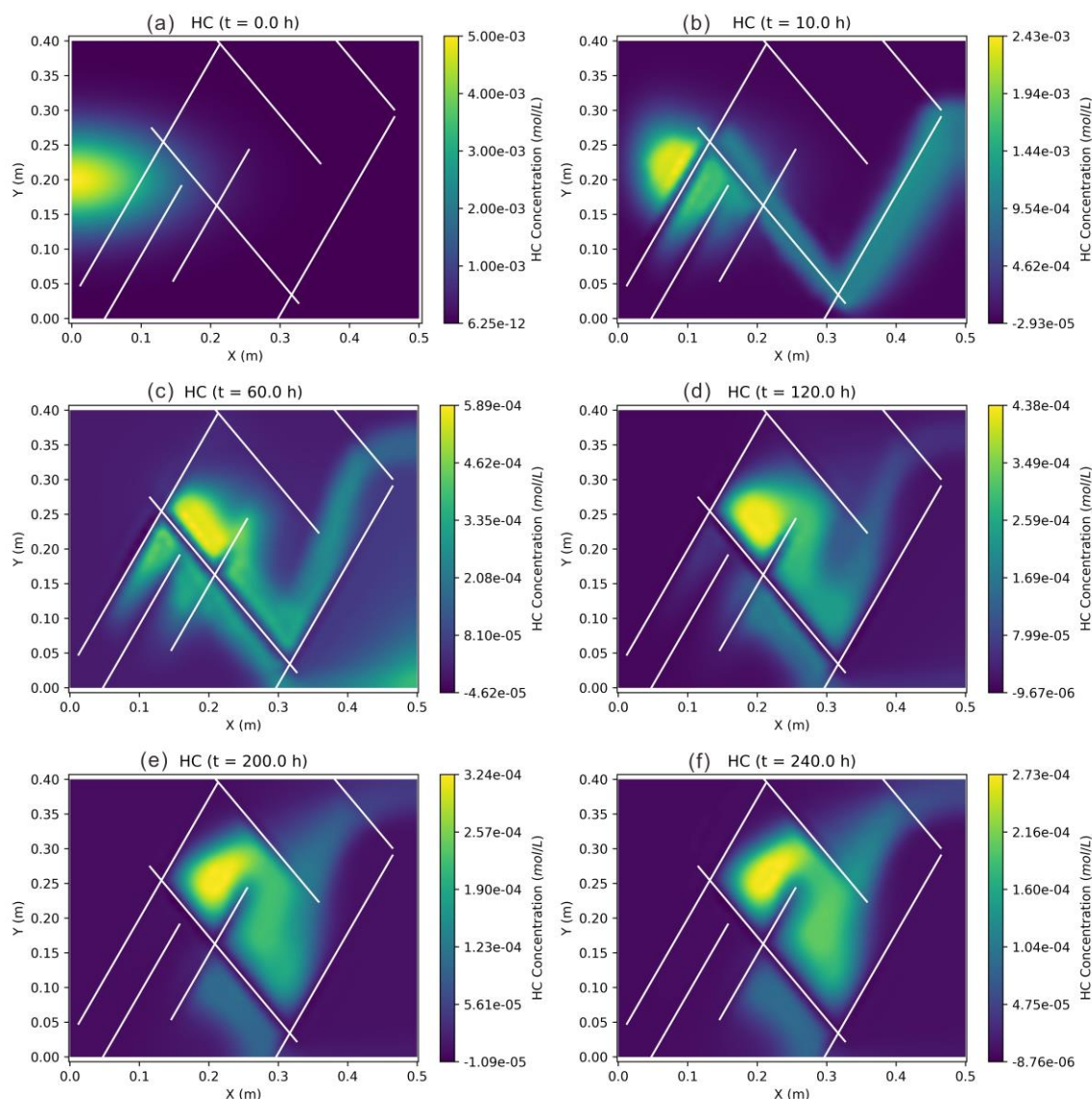


**Figure 6: Temporal evolution of Toluene (HC) concentration in the fractured aquifer domain. (a-f) HC concentration distributions at t=0,10,60,120,200,240h, respectively. White lines denote fractures. Colour indicates concentration (mol/L), showing advection-dispersion coupled with biogeochemical reactions within the matrix and along fracture pathways.**

475

The spatial distribution of primary species (Fig. 7) demonstrates that PHYGNET accurately captures the complex redox zonation within the fractured aquifer. The concentration profiles of  $O_2$  and  $NO_3^-$  reveal significant depletion zones precisely aligned with the high-permeability fracture network, where hydrocarbon degradation is most intensive. These sharp gradients at the fracture-matrix interface confirm the model's ability to simulate the rapid consumption of oxidants delivered via preferential flow paths, effectively resolving the localized biogeochemical fronts typical of heterogeneous media.

480



485

Conversely, the accumulation of  $\text{CH}_4$  and the synchronized shifts in pH and pe (Figs. 7d-f) highlight the model's biogeochemical consistency. The peak methane concentrations and reduced pe values are localized within the anaerobic plume core, reflecting the sequential utilization of electron acceptors and the onset of methanogenic conditions. This coherent correlation between oxidant depletion and metabolic by-product formation proves that PHYGNET maintains rigorous chemical logic and mass balance, successfully serving as a surrogate traditional solver while preserving high-fidelity spatial variations across the fractured domain.

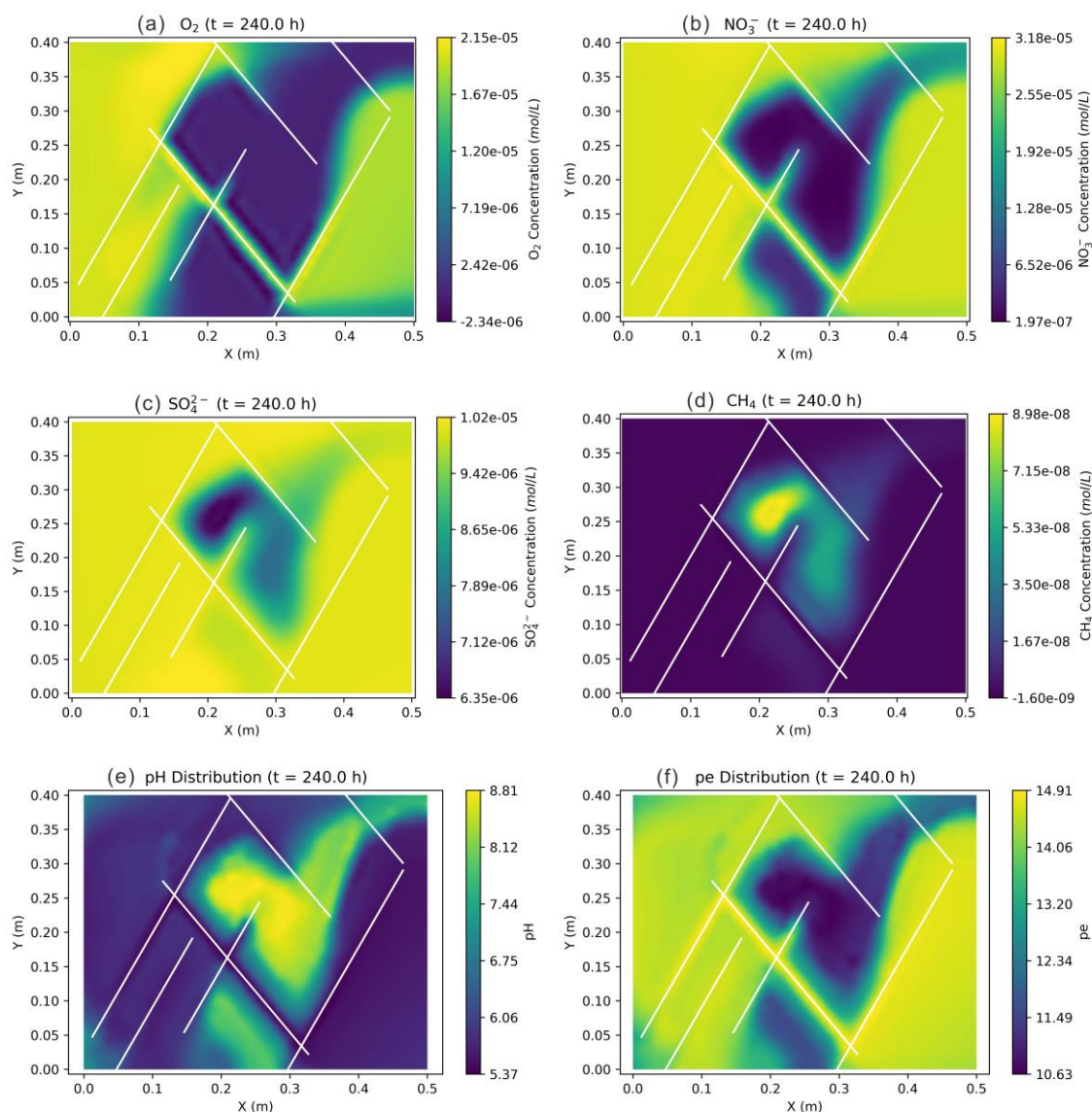


**Figure 7: Spatial distributions of major reactive species and geochemical indicators at the final simulation time. (a) Dissolved oxygen ( $\text{O}_2$ ) concentration (mol/L); (b) Nitrate ( $\text{NO}_3^-$ ) concentration (mol/L); (c) Sulfate ( $\text{SO}_4^{2-}$ ) concentration (mol/L); (d) Methane ( $\text{CH}_4$ ) concentration (mol/L); (e) pH distribution; (f) pe (redox potential) distribution.**

490



The spatial residual distributions at  $t = 240$  h (Figs. 8a-d) provide further evidence that the largest accumulated errors tend to occur at the final time step. The HC residuals remain localized and exhibit structured patterns aligned with the plume geometry, particularly near regions of strong concentration gradients and fracture intersections. Similar spatial coherence is observed in the pH and pe residual fields, where deviations are concentrated around chemically active zones rather than being randomly distributed. This indicates that PHYGNET preserves the spatial dependency between transport-driven concentration changes and reaction-induced geochemical responses.

Importantly, the residual patterns of pH and pe are consistent with the underlying redox dynamics. Areas with higher HC concentrations correspond to stronger deviations in redox indicators, reflecting intensified reaction activity. This spatial alignment confirms that PHYGNET correctly translates transport-induced variations in reactant availability into corresponding geochemical state updates, thereby maintaining the internal coupling between species transport and reaction processes.

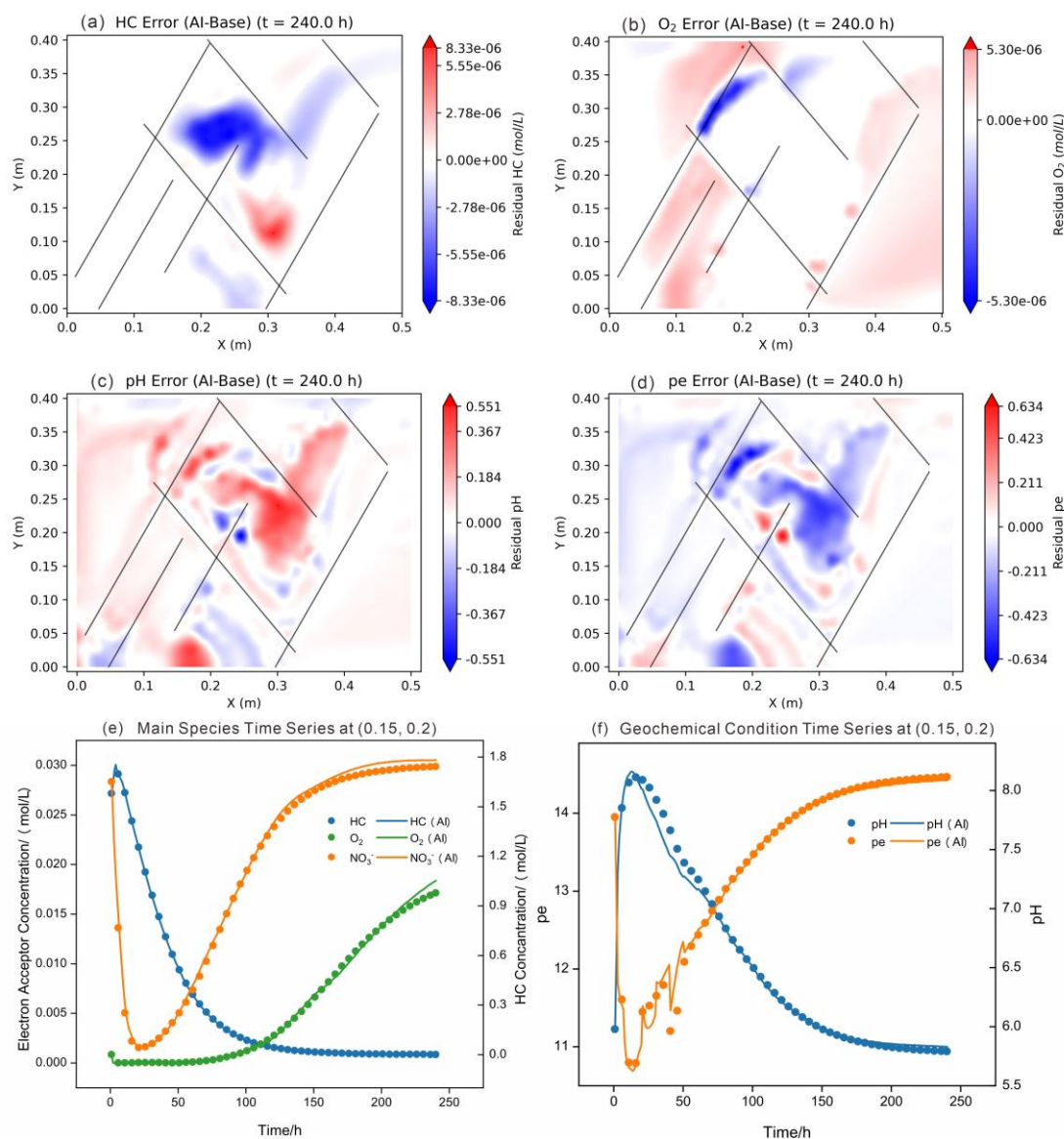


**Figure 8: PHYGNET-COMSOL coupling accuracy analysis. (a-d) Present the predicted residuals (AI - baseline) for HC concentration, O<sub>2</sub>, pH, and pe, respectively; (e-f) show the temporal evolution of major electron acceptors (O<sub>2</sub>, NO<sub>3</sub><sup>-</sup>) alongside pH and pe at representative observation points (0.15 m, 0.2 m).**

### 505 4.3 Surrogate Efficiency and Robustness

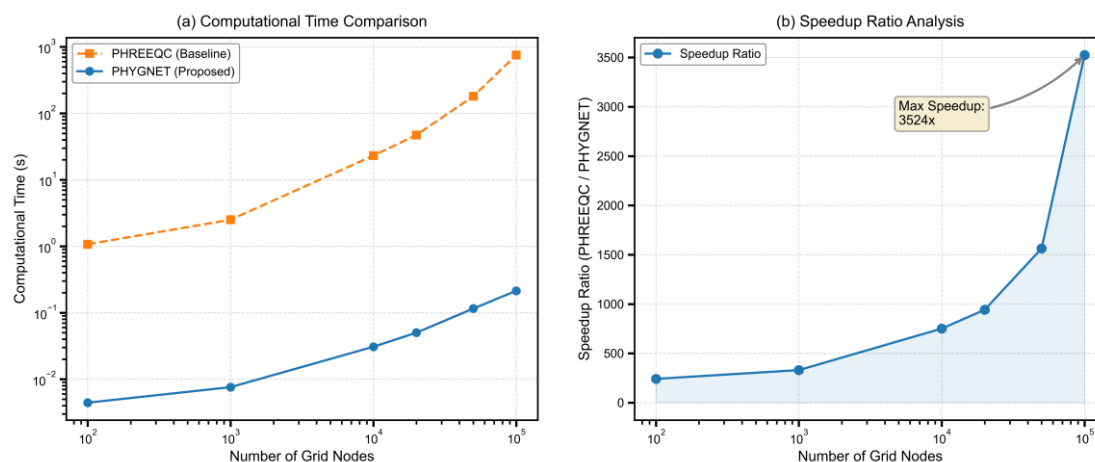
In comprehensive RTM involving kinetic reaction networks, geochemical solvers typically account for the vast majority of the total computational cost due to their complex nonlinear iterative solving mechanisms, and they frequently become the weak link that triggers computational crashes. To quantitatively evaluate the feasibility and performance limits of the PHYGNET surrogate in handling large-scale, three-dimensional site engineering problems, a rigorous benchmark test was conducted.



510 Utilizing realistic chemical state datasets generated during the coupled simulation, we compared the single-step computation time and stability of the traditional PHREEQC solver against PHYGNET under a broad range of computational loads (from  $10^2$  to  $10^5$  grid samples).

The benchmark results (Fig. 9a) first reveal a severe scalability bottleneck faced by traditional models when dealing with engineering-scale data. Traditional geochemical solvers primarily rely on serial computation modes and are highly dependent on dense, text-based I/O interactions. At smaller grid scales ( $N \leq 10,000$ ), the computation time of PHREEQC maintains a relatively linear growth (taking approximately 23.1 seconds). However, when the grid scale expands to 50,000 and 100,000 nodes, scales common in real-world site models, its computational overhead exhibits a significant super-linear increase in computational cost. Under the extreme stress test of  $N=100,000$ , overwhelmed by massive I/O congestion and the accumulated non-linear iteration time across the vast grid, PHREEQC's single-step solving time soared to 753.7 seconds (over 12.5 minutes).

520 For long-term engineering simulations that typically contain tens of thousands of time steps, this extremely low efficiency makes traditional solvers practically intractable. In contrast, PHYGNET accelerates and stabilizes the iterative loops and cumbersome file I/O mechanisms of traditional solvers, exploiting the tensor parallelism inherent in deep learning architectures. Through highly vectorized graph feature construction and forward inference, the model demonstrates exceptional computational scalability. Under the same hardware environment, PHYGNET takes only about 0.03 seconds to process 10,000 complex grids; even under the extreme load of 100,000 grids, its inference time remains remarkably stable at around 0.21 seconds. At this scale, PHYGNET achieves a 3524-fold acceleration compared to PHREEQC (Fig. 9b).



530 **Figure 9: Performance benchmark evaluating the computational efficiency and scalability of the proposed surrogate. (a) Comparison of single-step computational time between the traditional PHREEQC solver and PHYGNET. (b) The corresponding speedup ratio achieved by PHYGNET.**

More notably, as illustrated in Fig. 9b, the speedup ratio of PHYGNET relative to the traditional solver exhibits a significant and continuous upward trend as the number of simulation samples increases. This characteristic reveals a highly practical paradigm for engineering applications. By adopting a transfer learning approach, the framework can pre-train on foundational microbial kinetic topologies, entirely avoiding the inefficiencies of traditional knowledge distillation. When confronting large-



535 scale 3D site simulations comprising hundreds of thousands or even millions of grid nodes, it is entirely feasible to first employ  
a traditional solver (e.g., PHREEQC) to generate a limited number of representative small-scale samples to train the surrogate  
model, and subsequently delegate the remaining, overwhelmingly massive node computation tasks entirely to the trained  
PHYGNET. Because the surrogate model yields substantial computational dividends from tensor parallelism when processing  
large-scale data, this “small-sample training, ultra-large-scale inference” strategy effectively offsets the initial time costs  
540 incurred during training data generation. This monumental leap in efficiency implies that PHYGNET can compress large-scale  
uncertainty analyses (e.g., Monte Carlo simulations), which would traditionally require weeks of computation on  
supercomputing clusters, into a matter of hours on a standard workstation.

Beyond sheer computational speed, the numerical robustness exhibited by the surrogate model is another core value that breaks  
through the limitations of large-scale RTM applications. When processing real transport data involving multi-electron  
545 acceptors and extreme redox gradients (such as fracture-matrix interfaces), the Newton-Raphson iteration method employed  
by traditional solvers shows extreme fragility. When encountering local stiff kinetics or trace component concentrations  
approaching numerical limits, this mechanism is highly susceptible to falling into infinite iterative loops or crashing and  
reporting errors upon reaching the maximum number of iterations (e.g., 200 iterations). In a complex computational domain  
with hundreds of thousands of grids, the convergence failure of any single node will inevitably interrupt the entire coupled  
550 workflow. As a surrogate model based on continuous function mapping, PHYGNET’s inference process is completely  
decoupled from the iterative approximation mechanics of nonlinear equation systems. Consequently, even under highly  
heterogeneous chemical gradients in the input data, the network can compute features within a deterministic and extremely  
minuscule time window. Furthermore, under the dual safeguards of the hard-coded logic gating in the downstream Kinetics  
Layer and the smooth correction provided by the residual network (MLP), PHYGNET consistently and stably outputs bounded  
555 and reasonable results that strictly conform to mass conservation and thermodynamic hierarchies. In this benchmark test, even  
when concurrently subjected to the impact of 100,000 highly heterogeneous solution samples, PHYGNET achieved zero local  
crashes, zero memory overflows, and zero computational stalls. This quantum leap in efficiency coupled with outstanding  
numerical robustness fundamentally ensures the continuity and reliability of massive RTM simulations in complex porous and  
fractured media.

### 560 **4.3 Surrogate Interpretability**

In the PHYGNET architecture, predicted kinetic parameters function as learnable, physically plausible controls within Monod-  
type expressions. These parameters consistently align with traditional fixed values, demonstrating the model’s capacity to infer  
reasonable ranges for unknown parameters. To investigate how PHYGNET infers latent kinetic parameters from sparse  
concentration fields without explicit supervision, we applied Shapley Additive Explanations (SHAP) analysis (Lundberg and  
565 Lee, 2017) to the predicted logarithmic rate constants ( $\log k_{\max,i}$ ) and the residual correction terms. SHAP provides a  
theoretically grounded, game-theoretic attribution framework widely used to interpret machine-learning models in  
environmental and geoscience applications (Aldrees et al., 2025). The results are analysed as follows.



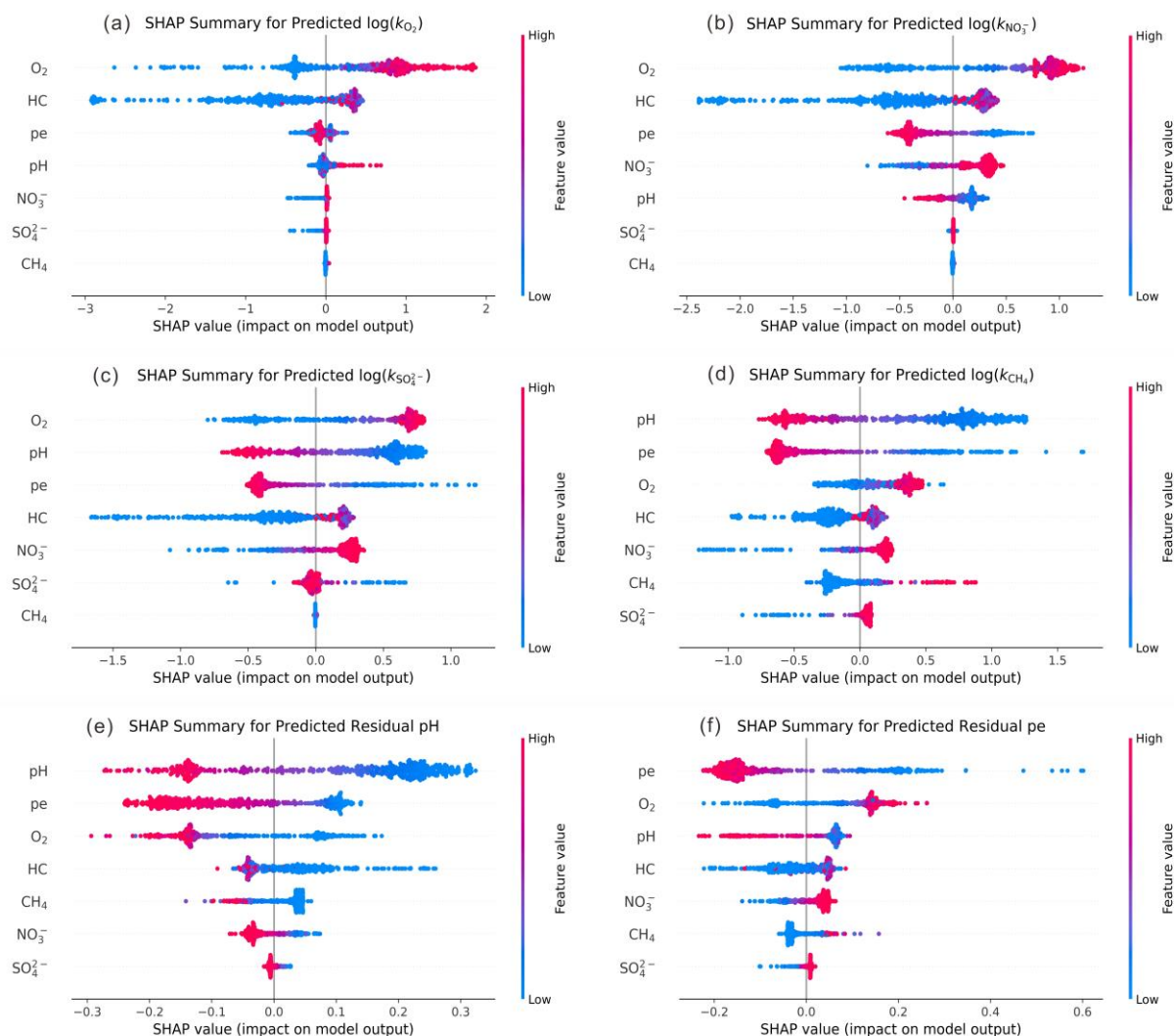
For the aerobic respiration rate constant  $\log(k_{O_2})$  (Fig. 10a), the SHAP summary indicates that substrate availability is the primary driver. High concentrations of dissolved  $O_2$  and HC, indicated by red points, correspond to positive SHAP values, thereby increasing the predicted rate parameter. This behaviour is fully consistent with Monod kinetics, where the reaction potential is maximized when both electron donors and acceptors are abundant (Monod, 1949). The GNN correctly identifies the plume core, where reagents are concentrated, as the zone of highest metabolic activity.

The aerobic pathway provides a clear example of substrate-driven behaviour. For the aerobic respiration rate constant  $\log(k_{O_2})$  (Fig. 10a), the SHAP summary plot shows strong positive contributions associated with high concentrations of dissolved  $O_2$  and HC. Regions containing both electron donors and electron acceptors therefore receive the largest upward shifts in predicted rate constants. This pattern aligns closely with classical Monod kinetics, in which reaction potential is maximized when both substrates are abundant (Monod, 1949). Consistent with this principle, the GNN component correctly identifies the hydrocarbon plume core as the region of highest metabolic activity, even under strong spatial heterogeneity.

In contrast, anaerobic pathways including denitrification and sulfate reduction (Figs. 10b-c) display an apparently counterintuitive SHAP pattern: inhibitors such as  $O_2$  and  $NO_3^-$  show positive contributions to the predicted rate constants. For instance, higher concentrations of  $O_2$  correlate with larger  $\log(k_{SO_4^{2-}})$  values, despite the fact that sulfate reduction should be thermodynamically suppressed under oxidizing conditions. This behaviour does not necessarily indicate model error; rather, it reflects the cooperative structure of PHYGNET's hybrid architecture. The GNN serves as a "resource recognizer", leveraging persistent spatial correlations in the plume. Zones with high concentrations of supposed inhibitors often coincide with the advancing plume front, where HC and other reactants remain abundant. The GNN learns to interpret these high-concentration signals as markers of high reaction potential, producing correspondingly high estimates of the maximum rate constant. Crucially, these predictions do not directly determine the final reaction rate. The downstream physics-based kinetics layer imposes explicit Monod inhibition terms, which strictly enforce thermodynamic hierarchy. Even if the GNN predicts a high  $k_{rate}$  in oxic zones, the kinetics layer mathematically drives the actual reaction rate toward zero. This synergy effectively separates the tasks of "locating potential reactivity" and "enforcing thermodynamic feasibility", reducing the learning burden and improving stability in kinetic reaction systems.

SHAP analysis of the residual correction terms for pH and pe (Figs. 10e-f) further reveals a consistent negative correlation pattern, when the state variable is high, the residual network tends to output a negative adjustment. This indicates that the lightweight MLP acts as a "steady-state buffer", mimicking acid-base and redox buffering processes commonly observed in natural waters. By compensating for linearization errors in the physics layer, the residual network keeps the predicted system within chemically reasonable bounds and prevents long-term numerical drift.

Taken together, these interpretability results demonstrate that PHYGNET possesses strong physical reasoning capabilities. Its architecture successfully decouples the tasks of detecting spatial patterns of reaction potential (handled by the GNN) and enforcing biogeochemical constraints (handled by the physics layer), while the residual network provides fine-scale stabilizing adjustments. This hybrid mechanism enables accurate, stable, and interpretable simulation of reactive transport in complex multi-electron-acceptor environments.



605 **Figure 10: SHAP summary plots revealing the autonomous learning of biogeochemical mechanisms by PHYGNET. The analysis decomposes the drivers for (a-d) predicted kinetic rate parameters ( $\log k_{\max,i}$ ) and (e-f) residual corrections. (a) Aerobic respiration is correctly driven by substrate availability ( $O_2$  and HC). (b-d) For anaerobic pathways, theoretical inhibitors (e.g.,  $O_2$  for denitrification) exhibit positive SHAP contributions. (e-f) Residual corrections for pH and pe show a negative correlation with their respective state variables.**

## 5 Conclusions

610 This study introduces PHYGNET, a physically integrated Graph Neural Network (GNN) framework designed to serve as an efficient, interpretable, and highly robust surrogate for biogeochemical solvers in reactive transport models (RTMs). By integrating a metabolic-structured GNN architecture with an explicit Monod-based kinetic physics layer and a residual corrector, PHYGNET successfully overcomes the intrinsic limitations of pure data-driven black-box models. It accurately



captures the stiff, nonlinear dynamics of microbially-mediated kinetic reaction degradation systems while strictly enforcing elemental mass conservation and thermodynamic hierarchies.

615 Interpretability analyses via SHAP confirm that PHYGNET captures intuitive and mechanistically consistent trends in how local substrate concentration and redox conditions affect reaction rates. The GNN effectively acts as a spatial “resource recognizer” for metabolic reaction potentials, while the downstream physics layer guarantees thermodynamic feasibility, providing a transparent and trustworthy AI-physics synergy.

When embedded into a COMSOL-coupled RTM framework, PHYGNET demonstrated exceptional performance in simulating  
620 complex plume evolution and biological redox zonation within a highly heterogeneous fractured aquifer. Crucially, rigorous benchmark testing revealed that PHYGNET could alleviate the computational burden associated with high-dimensional systems and numerical stiffness that plague traditional solvers. While conventional tools such as PHREEQC suffer from super-linear time penalties and convergence failures at engineering scales, PHYGNET exploits tensor parallelism to maintain stable sub-linear scaling. At a massive scale of 100,000 grid nodes, the surrogate achieved an unprecedented 3524-fold computational  
625 acceleration with zero numerical crashes. Furthermore, the continuous upward trend of the speedup ratio with increasing computational scale establishes a highly practical engineering paradigm, utilizing a small number of samples generated by traditional solvers for training, followed by ultra-large-scale inference on millions of nodes. This strategy effectively offsets the initial time costs of data generation and maximizes the dividends of tensor parallelism.

Beyond efficiency gains, the model’s modular design supports easy adaptation to new transport boundary conditions,  
630 contaminants, and microbial metabolic pathways, offering broad utility for large-scale environmental bioremediation simulations. By compressing the computational time of large-scale RTMs from weeks to a matter of hours, this work provides a promising pathway for addressing previously intractable tasks (such as high-resolution 3D site modelling, real-time remediation optimization, and comprehensive uncertainty quantification), marking a significant step forward in the real-world application of reactive transport modelling.

635 Despite these capabilities, we acknowledge certain limitations in the current study that outline the trajectory for future research. Presently, the performance and stability of the PHYGNET framework have been rigorously validated primarily within synthetic, albeit highly heterogeneous, 2D fractured domains. Additionally, the current physics layer is exclusively tailored for Monod-type biological kinetics and does not yet explicitly resolve concurrent inorganic processes such as mineral dissolution-precipitation. Therefore, our forthcoming work will focus on expanding the differentiable physics library to  
640 encompass a wider range of geochemical formulations, and deploying PHYGNET at a full-scale, three-dimensional real-world field site.

### Code and data availability

The code and data generated for this study are available in the Zenodo repository at (Wang, 2025) <https://doi.org/10.5281/zenodo.17797476>. Further inquiries can be directed to the corresponding author.



645

### **Author contributions**

650 Jinbo Wang: conceptualization, writing - original draft, methodology and visualization. Kunfeng Zhang: software. Jinbo Wang, Kunfeng Zhang: formal analysis. Walter Illman, Mingzhu Liu: supervision. Mingzhu Liu: investigation. Walter Illman, Shuai Chen, Mingzhu Liu: writing - reviewing & editing. Mingzhu Liu: funding acquisition

### **Competing interests**

The contact author has declared that none of the authors has any competing interests.

### 655 **Disclaimer**

Copernicus Publications remains neutral with regard to jurisdictional claims made in the text, published maps, institutional affiliations, or any other geographical representation in this paper. While Copernicus Publications makes every effort to include appropriate place names, the final responsibility lies with the authors. Views expressed in the text are those of the authors and do not necessarily reflect the views of the publisher.

### 660 **Acknowledgements**

This work was supported by the Jing-Jin-Ji Regional Integrated Environmental Improvement-National Science and Technology Major Project (2025ZD1205700). Walter A. Illman acknowledges the partial support from the Discovery grant funded by the Natural Sciences and Engineering Research Council of Canada (NSERC) which facilitated this collaboration.

### **Financial support**

665 This work was supported by the Jing-Jin-Ji Regional Integrated Environmental Improvement-National Science and Technology Major Project (2025ZD1205700).



## 670 References

- Aldreess, A., Jibrin, A. M., Dan'azumi, S., Mahmoud, I. A., Aliyu, U. U., and Abba, S. I.: Explainable machine learning framework for assessing groundwater quality and trace element contamination in Eastern Saudi Arabia, *Sci Rep*, <https://doi.org/10.1038/s41598-025-29598-8>, 2025.
- Brookfield, A. E., Ajami, H., Carroll, R. W. H., Tague, C., Sullivan, P. L., and Condon, L. E.: Recent advances in integrated hydrologic models: Integration of new domains, *Journal of Hydrology*, 620, 129515, <https://doi.org/10.1016/j.jhydrol.2023.129515>, 2023.
- Chen, C., Deng, Y., Qian, J., Ma, H., Ma, L., Wu, J., and Wu, H.: Deep learning-based inversion framework for fractured media characterization by assimilating hydraulic tomography and thermal tracer tomography data: Numerical and field study, *Engineering Geology*, 350, 107998, <https://doi.org/10.1016/j.enggeo.2025.107998>, 2025.
- 675 De Lucia, M. and Kühn, M.: DecTree v1.0 - chemistry speedup in reactive transport simulations: purely data-driven and physics-based surrogates, *Geoscientific Model Development*, 14, 4713-4730, <https://doi.org/10.5194/gmd-14-4713-2021>, 2021.
- Demirer, E., Coene, E., Iraola, A., Nardi, A., Abarca, E., Idiart, A., de Paola, G., and Rodríguez-Morillas, N.: Improving the performance of reactive transport simulations using artificial neural networks, *Transp Porous Med*, 149, 271-297, <https://doi.org/10.1007/s11242-022-01856-7>, 2023.
- 685 Deng, F., Wu, J., Yang, Y., Li, J., Xie, X., Jiang, J., and Zhu, X.: Improved physics-informed neural network for reactive transport modeling of groundwater arsenic enrichment, *Sci. China Earth Sci.*, 68, 2781-2796, <https://doi.org/10.1007/s11430-024-1590-x>, 2025.
- Falkowski, P. G., Fenchel, T., and Delong, E. F.: The Microbial Engines That Drive Earth's Biogeochemical Cycles, *Science*, 690 320, 1034-1039, <https://doi.org/10.1126/science.1153213>, 2008.
- Fotherby, A., Bradbury, H. J., Druhan, J. L., and Turchyn, A. V.: An emulation-based approach for interrogating reactive transport models, *Geoscientific Model Development*, 16, 7059-7074, <https://doi.org/10.5194/gmd-16-7059-2023>, 2023.
- Hammond, G. E., Lichtner, P. C., and Mills, R. T.: Evaluating the performance of parallel subsurface simulators: An illustrative example with PFLOTRAN, *Water Resources Research*, 50, 208-228, <https://doi.org/10.1002/2012WR013483>, 2014.
- 695 He, W., Beyer, C., Fleckenstein, J. H., Jang, E., Kolditz, O., Naumov, D., and Kalbacher, T.: A parallelization scheme to simulate reactive transport in the subsurface environment with OGS#IPhreeqc 5.5.7-3.1.2, *Geoscientific Model Development*, 8, 3333-3348, <https://doi.org/10.5194/gmd-8-3333-2015>, 2015.



- Hyman, J. D. and Jimenez-Martinez, J.: Dispersion and mixing in three-dimensional discrete fracture networks: nonlinear  
interplay between structural and hydraulic heterogeneity, *Water Resour. Res.*, 54, 3243-3258,  
700 <https://doi.org/10.1029/2018WR022585>, 2018.
- Hyman, J. D., Hagberg, A., Srinivasan, G., Mohd-Yusof, J., and Viswanathan, H.: Predictions of first passage times in sparse  
discrete fracture networks using graph-based reductions, *Phys. Rev. E*, 96, 013304,  
<https://doi.org/10.1103/PhysRevE.96.013304>, 2017.
- Jatnieks, J., De Lucia, M., Dransch, D., and Sips, M.: Data-driven surrogate model approach for improving the performance  
705 of reactive transport simulations, *Energy Procedia*, 97, 447-453, <https://doi.org/10.1016/j.egypro.2016.10.047>, 2016.
- Jiang, S., Zheng, Y., and Solomatine, D.: Improving AI system awareness of geoscience knowledge: symbiotic integration of  
physical approaches and deep learning, *Geophysical Research Letters*, 47, e2020GL088229,  
<https://doi.org/10.1029/2020GL088229>, 2020.
- Johnson, K. A. and Goody, R. S.: The Original Michaelis Constant: Translation of the 1913 Michaelis-Menten Paper,  
710 *Biochemistry*, 50, 8264-8269, <https://doi.org/10.1021/bi201284u>, 2011.
- Keller, C. A. and Evans, M. J.: Application of random forest regression to the calculation of gas-phase chemistry within the  
GEOS-Chem chemistry model v10, *Geoscientific Model Development*, 12, 1209-1225, <https://doi.org/10.5194/gmd-12-1209-2019>, 2019.
- Kim, S., Lee, E., Hwang, H.-T., Pyo, J., Yun, D., Baek, S.-S., and Cho, K. H.: Spatiotemporal estimation of groundwater and  
715 surface water conditions by integrating deep learning and physics-based watershed models, *Water Res. X*, 23, 100228,  
<https://doi.org/10.1016/j.wroa.2024.100228>, 2024.
- Koehn, D., Piazzolo, S., Beaudoin, N. E., Kelka, U., Spruženiece, L., Putnis, C. V., and Toussaint, R.: Relative rates of fluid  
advection, elemental diffusion and replacement govern reaction front patterns, *Earth and Planetary Science Letters*, 565,  
116950, <https://doi.org/10.1016/j.epsl.2021.116950>, 2021.
- 720 Laloy, E. and Jacques, D.: Speeding up reactive transport simulations in cement systems by surrogate geochemical modeling:  
deep neural networks and k-nearest neighbors, *Transp Porous Med*, 143, 433-462, <https://doi.org/10.1007/s11242-022-01779-3>, 2022.
- Li, L., Steefel, C. I., and Yang, L.: Scale dependence of mineral dissolution rates within single pores and fractures, *Geochimica  
et Cosmochimica Acta*, 72, 360-377, <https://doi.org/10.1016/j.gca.2007.10.027>, 2008.
- 725 Lundberg, S. M. and Lee, S.-I.: A unified approach to interpreting model predictions, in: *Proceedings of the 31st International  
Conference on Neural Information Processing Systems*, 4768-4777, 2017.
- Luo, C., Wang, X., Xu, Y. J., Jia, S., Liu, Z., Mao, B., Lv, Q., Ji, X., Rong, Y., and Dai, Y.: Synergistic identification of  
hydrogeological parameters and pollution source information for groundwater point and areal source contamination based on  
machine learning surrogate-artificial hummingbird algorithm, *Hydrology and Earth System Sciences*, 29, 5719-5736,  
730 <https://doi.org/10.5194/hess-29-5719-2025>, 2025.



- Mayer, K. U., Frind, E. O., and Blowes, D. W.: Multicomponent reactive transport modeling in variably saturated porous media using a generalized formulation for kinetically controlled reactions, *Water Resources Research*, 38, 13-1-13-21, <https://doi.org/10.1029/2001WR000862>, 2002.
- McGovern, A., Lagerquist, R., John Gagne, D., Jergensen, G. E., Elmore, K. L., Homeyer, C. R., and Smith, T.: Making the  
735 black box more transparent: understanding the physical implications of machine learning, *Bulletin of the American Meteorological Society*, 100, 2175-2199, <https://doi.org/10.1175/BAMS-D-18-0195.1>, 2019.
- Meile, C. and Scheibe, T. D.: Reactive Transport Modeling of Microbial Dynamics, *Elements*, 15, 111-116, <https://doi.org/10.2138/gselements.15.2.111>, 2019.
- Midlagajni, N. and Rothkopf, C. A.: Graph neural networks for learning liquid simulations in dynamic scenes containing  
740 kinematic objects, <https://doi.org/10.48550/arXiv.2509.03446>, 2025.
- Mo, S., Zabarar, N., Shi, X., and Wu, J.: Deep autoregressive neural networks for high-dimensional inverse problems in groundwater contaminant source identification, *Water Resources Research*, 55, 3856-3881, <https://doi.org/10.1029/2018WR024638>, 2019.
- Monod, J.: The growth of bacterial cultures, *Annual Review of Microbiology*, 3, 371-394,  
745 <https://doi.org/10.1146/annurev.mi.03.100149.002103>, 1949.
- Pang, M., Du, E., and Zheng, C.: Contaminant transport modeling and source attribution with attention-based graph neural network, *Water Resources Research*, 60, e2023WR035278, <https://doi.org/10.1029/2023WR035278>, 2024.
- Prommer, H. and Stuyfzand, P. J.: Identification of temperature-dependent water quality changes during a deep well aquifer, *Environ. Sci. Technol.*, 39, 2200-2209, <https://doi.org/10.1021/es0486768>, 2005.
- 750 Reiser, P., Neubert, M., Eberhard, A., Torresi, L., Zhou, C., Shao, C., Metni, H., van Hoesel, C., Schopmans, H., Sommer, T., and Friederich, P.: Graph neural networks for materials science and chemistry, *Commun Mater*, 3, 93, <https://doi.org/10.1038/s43246-022-00315-6>, 2022.
- Rudin, C.: Stop explaining black box machine learning models for high stakes decisions and use interpretable models instead, *Nat Mach Intell*, 1, 206-215, <https://doi.org/10.1038/s42256-019-0048-x>, 2019.
- 755 Shi, X., Ye, M., Curtis, G. P., Miller, G. L., Meyer, P. D., Kohler, M., Yabusaki, S., and Wu, J.: Assessment of parametric uncertainty for groundwater reactive transport modeling, *Water Resour. Res.*, 50, 4416-4439, <https://doi.org/10.1002/2013WR013755>, 2014.
- Silva, V. L. S., Regnier, G., Salinas, P., Heaney, C. E., Jackson, M. D., and Pain, C. C.: Rapid modelling of reactive transport in porous media using machine learning: limitations and solutions, <https://doi.org/10.48550/arXiv.2405.14548>, 2025.
- 760 Solgi, R., Loáiciga, H. A., and Kram, M.: Long short-term memory neural network (LSTM-NN) for aquifer level time series forecasting using in-situ piezometric observations, *Journal of Hydrology*, 601, 126800, <https://doi.org/10.1016/j.jhydrol.2021.126800>, 2021.



- Sprocati, R. and Rolle, M.: Integrating process-based reactive transport modeling and machine learning for electrokinetic remediation of contaminated groundwater, *Water Resources Research*, 57, e2021WR029959, <https://doi.org/10.1029/2021WR029959>, 2021.
- 765 Steefel, C. I., Appelo, C. A. J., Arora, B., Jacques, D., Kalbacher, T., Kolditz, O., Lagneau, V., Lichtner, P. C., Mayer, K. U., Meeussen, J. C. L., Molins, S., Moulton, D., Shao, H., Šimůnek, J., Spycher, N., Yabusaki, S. B., and Yeh, G. T.: Reactive transport codes for subsurface environmental simulation, *Comput Geosci*, 19, 445-478, <https://doi.org/10.1007/s10596-014-9443-x>, 2015.
- 770 Sturm, P. O. and Wexler, A. S.: Conservation laws in a neural network architecture: enforcing the atom balance of a Julia-based photochemical model (v0.2.0), *Geoscientific Model Development*, 15, 3417-3431, <https://doi.org/10.5194/gmd-15-3417-2022>, 2022.
- Veličković, P., Cucurull, G., Casanova, A., Romero, A., Liò, P., and Bengio, Y.: Graph Attention Networks, <https://doi.org/10.48550/arXiv.1710.10903>, 2018.
- 775 Wang, J.: Code and data for PHYGNET, , <https://doi.org/10.5281/zenodo.17797476>, 2025.
- Wang, J., Ren, L., Zhang, K., Zhang, C., Zhang, Y., and Liu, M.: Multi-task neural network combined with multi-source data for inversion of discrete fracture network apertures: Aperture-XNET, *Journal of Hydrology*, 661, 133584, <https://doi.org/10.1016/j.jhydrol.2025.133584>, 2025a.
- Wang, Z., Li, W., Wang, S., and Wang, X.: The Future of Catalysis: Applying Graph Neural Networks for Intelligent Catalyst Design, *WIREs Computational Molecular Science*, 15, e70010, <https://doi.org/10.1002/wcms.70010>, 2025b.
- 780 Wei, Y. and Cao, X.: A COMSOL-PHREEQC coupled Python framework for reactive transport modeling in soil and groundwater, *Groundwater*, 60, 284-294, <https://doi.org/10.1111/gwat.13144>, 2022.
- Wu, Z., Yao, Y., Guo, S., Yang, S., He, X., Lancia, M., and Zheng, C.: Graph fourier deep learning for spatiotemporal and hydrogeological interpretation of groundwater levels in the yellow river basin, *Water Resources Research*, 61, e2025WR041215, <https://doi.org/10.1029/2025WR041215>, 2025.
- 785 Xu, Y., Lu, W., Pan, Z., and Wang, Z.: Framework for identification of groundwater contamination source based on conditional generative adversarial networks and optimization methods, *Water Resources Research*, 61, e2024WR039467, <https://doi.org/10.1029/2024WR039467>, 2025.
- Zeng, X., Xiang, H., Yu, L., Wang, J., Li, K., Nussinov, R., and Cheng, F.: Accurate prediction of molecular properties and drug targets using a self-supervised image representation learning framework, *Nat Mach Intell*, 4, 1004-1016, <https://doi.org/10.1038/s42256-022-00557-6>, 2022.
- 790 Zhan, C., Dai, Z., Yang, Z., Zhang, X., Ma, Z., Thanh, H. V., and Soltanian, M. R.: Subsurface sedimentary structure identification using deep learning: A review, *Earth-Science Reviews*, 239, 104370, <https://doi.org/10.1016/j.earscirev.2023.104370>, 2023.